

# JGR Solid Earth

## RESEARCH ARTICLE

10.1029/2024JB029918

### Key Points:

- A novel eikonal equation-based adjoint-state reflection traveltome tomography method is proposed
- The Fréchet derivatives for interface topography and velocity structure are explicitly derived
- Low-velocity anomalies imaged in the lower crust of central California near Parkfield suggest the presence of fluids

### Supporting Information:

Supporting Information may be found in the online version of this article.

### Correspondence to:

P. Tong,  
tongping@ntu.edu.sg

### Citation:

Chen, G., Chen, J., Li, T., Xu, M., Zhao, Q., & Tong, P. (2025). Adjoint-state reflection traveltome tomography for velocity and interface inversion with its application in central California near Parkfield. *Journal of Geophysical Research: Solid Earth*, 130, e2024JB029918. <https://doi.org/10.1029/2024JB029918>

Received 31 JUL 2024

Accepted 25 DEC 2024

### Author Contributions:

**Conceptualization:** Guoxu Chen, Jing Chen, Ping Tong  
**Data curation:** Guoxu Chen, Tianjue Li  
**Formal analysis:** Guoxu Chen, Jing Chen  
**Funding acquisition:** Qi Zhao, Ping Tong  
**Investigation:** Guoxu Chen  
**Methodology:** Guoxu Chen, Jing Chen, Ping Tong  
**Project administration:** Ping Tong  
**Software:** Guoxu Chen, Tianjue Li, Mijian Xu  
**Supervision:** Qi Zhao, Ping Tong  
**Validation:** Guoxu Chen, Ping Tong  
**Visualization:** Guoxu Chen, Tianjue Li  
**Writing – original draft:** Guoxu Chen  
**Writing – review & editing:** Jing Chen, Tianjue Li, Mijian Xu, Qi Zhao, Ping Tong

## Adjoint-State Reflection Traveltome Tomography for Velocity and Interface Inversion With Its Application in Central California Near Parkfield

Guoxu Chen<sup>1,2</sup> , Jing Chen<sup>2</sup> , Tianjue Li<sup>2</sup> , Mijian Xu<sup>2</sup> , Qi Zhao<sup>1</sup> , and Ping Tong<sup>2,3,4</sup> 

<sup>1</sup>Department of Civil and Environmental Engineering, The Hong Kong Polytechnic University, Hong Kong, China, <sup>2</sup>School of Physical and Mathematical Sciences, Nanyang Technological University, Singapore, Singapore, <sup>3</sup>Earth Observatory of Singapore, Nanyang Technological University, Singapore, Singapore, <sup>4</sup>Asian School of the Environment, Nanyang Technological University, Singapore, Singapore

**Abstract** Traveltome tomography considering reflection arrivals is a promising approach for investigating interface topography and near-interface velocity heterogeneity. In this study, we formulate this inverse problem as an eikonal equation-constrained optimization problem, in which the traveltome field of the reflection wave is accurately described by a two-stage eikonal equation. The novelty lies in deriving the Fréchet derivative with respect to interface topography. By employing the coordinate transformation technique to convert an irregular physical domain with an undulating interface to a regular computational domain, we successfully encode the interface topography into the anisotropic parameters in the eikonal equation. This approach enables us to derive explicit forms of the Fréchet derivatives related to interface topography and velocity based on the adjoint-state method, which is not only computationally efficient but also avoids potential inaccuracy in ray tracing. Several numerical experiments are conducted to verify our new method. Finally, we apply this method to central California near Parkfield by inverting traveltimes of both first-P and Moho-reflected waves (named PmP). The low-velocity anomalies imaged in the lower crust are consistent with the along-strike variations of low-frequency earthquakes (LFEs) beneath the San Andreas Fault (SAF), suggesting the presence of fluids that may influence the occurrence of LFEs in this region.

**Plain Language Summary** Reflection traveltome tomography utilizes the arrival times of reflection waves to constrain subsurface structures. Reflection waves are more sensitive to deep velocity structures and interface positions compared to direct waves, thereby providing independent and valuable constraints on subsurface structures. This paper presents a framework for velocity and interface inversion by inverting reflection arrivals. For forward modeling, the propagation of reflection waves is described by a two-stage eikonal equation. We achieve high-precision calculation of the reflection arrivals by introducing appropriate coordinate transformations to equivalently convert undulating interfaces into anisotropic parameters. For inversion, explicit expressions of the sensitivity kernels of the misfit function with respect to both velocity structure and interface topography are derived based on the adjoint-state method. The entire workflow does not require ray tracing or wave equation solving. Finally, the effectiveness of the proposed method is demonstrated through a case study conducted in central California near Parkfield.

## 1. Introduction

Seismic tomography is one of the main tools for studying the heterogeneous structure of the Earth's interior. Following the pioneering work of Aki and Lee (1976), numerous tomographic imaging results of various scales have been obtained, which impact the study of geodynamic evolution, volcanism, and plate tectonics (e.g., Dziewonski et al., 1977; Tape et al., 2009; Van der Hilst et al., 1997; H. Zhu et al., 2012). Traveltome tomography is frequently utilized for illuminating subsurface velocity structures. In regional-scale traveltome tomography, studies based on first-P arrivals dominate because their traveltimes are one of the most robust information we can extract from seismic records. Given that the majority of intracrustal earthquakes occur in upper crust (Jackson et al., 2021), the tomographic resolution of lower crust is restricted due to insufficient data sampling, if only first-P arrivals are considered in inversion. Therefore, it is promising to consider crustal reflection arrivals (such as PmP, SmS, etc.) in traveltome tomography because they can provide unique constraints on the lower crust structure and Moho discontinuity, thereby improving imaging resolution (e.g., Christeson et al., 2013; Helmberger et al., 2001; Salah et al., 2005; Wang et al., 2022; Wu et al., 2022; D. Zhao et al., 2005).

Tong (2021a) has developed an eikonal equation-based adjoint-state traveltome tomography method, which can effectively determine subsurface velocity heterogeneity by inverting first arrivals. In comparison to ray tracing-based methods, the traveltome calculation based on solving an eikonal equation is more stable as it provides the minimum traveltome from the source to any location within the study region, enabling it to accurately compute first arrivals even in highly heterogeneous media. The computational cost is also acceptable, considering that commonly used techniques such as fast marching method (Sethian, 1999; Sethian & Vladimirsky, 2000) or fast sweeping method (Tsai et al., 2003; H. Zhao, 2005) can determine the traveltome field with a computational complexity of  $O(N \log N)$  or  $O(N)$ , where  $N$  refers to the total number of grid points in a discretized region. In contrast to waveform-based traveltome tomography methods, the computational complexity of solving a wave equation is approximately  $O(NN_t)$ , where  $N$  and  $N_t$  represent the number of spatial and temporal discretization grid points, respectively. The discretization parameters should be carefully determined based on the considered frequency and stability conditions, making solving high-frequency wave equations very time-consuming (Courant et al., 1967; Koene et al., 2018; Komatitsch & Tromp, 1999). Wave equations can be simplified to eikonal equations under the high-frequency assumption. So, similar to ray tracing-based methods, eikonal equation-based methods cannot characterize the finite frequency effect of seismic waves. Nevertheless, it achieves a good balance between computational efficiency and accuracy, making it ideal for traveltome tomography. However, Tong's method is only applicable to first arrivals and cannot be directly applied to the inversion of reflection arrivals. This study will construct an inversion framework for reflection arrivals based on a multi-stage eikonal equation and the adjoint-state method.

This study focuses on utilizing reflection arrivals to constrain velocity structures and interface topographies through forward modeling based on a two-stage eikonal equation and inversion with the adjoint-state method. Reflection arrivals have completely different propagation paths from first arrivals and carry valuable information about deep structures and reflector geometries, which can significantly improve tomographic resolution (e.g., Knapp et al., 2004; Li et al., 2022; Xia et al., 2007). Although solving an eikonal equation can typically only predict first-arrival traveltimes, the combination with a multi-stage scheme enables the calculation of reflection arrivals within heterogeneous models (Huang & Bellefleur, 2012; Rawlinson & Sambridge, 2004b). An important benefit is that its computational cost is proportional to the number of sources or receivers if reciprocity principle (Aki & Richards, 2002) is utilized. Specifically, the computational cost is reduced compared to methods based on Fermat's principle of stationary time. The latter requires calculating the traveltome field originating from each source and receiver to determine reflection arrivals (Podvin & Lecomte, 1991; Rawlinson & Sambridge, 2004a; Riahi & Juhlin, 1994). Besides, inspired by the topography-dependent eikonal solver (G. Guo et al., 2022; Lan & Zhang, 2013; Zhou et al., 2023), we can flatten the undulating interface by the coordinate transformation between the irregular physical domain and the regular computational domain. Such a transformation can equivalently convert interface topography into anisotropic parameters. Consequently, we can effectively solve anisotropic eikonal equations on a regularly discretized grid in the computational domain, which avoids the loss of accuracy that may be caused by irregular grids in the physical domain (Lan & Zhang, 2013). Combining these two approaches allows for the rapid and accurate computation of synthetic reflection arrivals. For the inversion, we derive Fréchet derivatives (or sensitivity kernels) of the misfit function with respect to velocity and interface topography, respectively, based on the adjoint-state method (J. Chen et al., 2023; Plessix, 2006; Tong, 2021a). In particular, since the undulating interface is fully described by the anisotropic parameters determined by the coordinate transformation, we can use these intermediate parameters to explicitly derive the gradient of the misfit function with respect to interface topography. The resulting sensitivity kernel can be combined with a gradient-based optimization method to iteratively determine optimal model parameters. In each iteration, only  $N_s$  (number of sources) forward simulations and  $N_s$  adjoint simulations are required to determine the gradient without the need for ray tracing.

The rest of this paper is arranged as follows. First, we introduce the proposed adjoint-state reflection traveltome tomography method in detail in Section 2, which describes the calculation of reflection arrivals and the derivation of the Fréchet derivatives based on the adjoint-state method. Then in Section 3, several numerical tests are performed to illustrate the effectiveness of the method. Finally, we apply the proposed method in central California near Parkfield. Through the alternating inversion of first-P arrivals and Moho-reflected PmP arrivals, the self-consistent subsurface velocity structure and Moho discontinuity models of the study region are constructed.

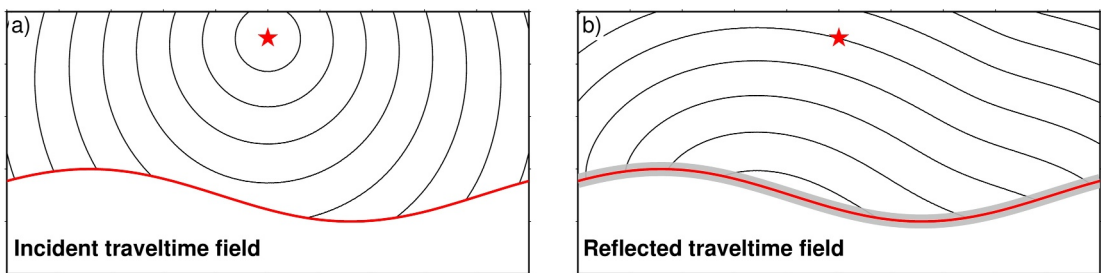


**Figure 1.** Schematic of travelttime field calculation. The red star is the source and the red curve marks the undulating reflection interface. (a) The incident travelttime field by solving Equation 1. (b) The reflected travelttime field by solving Equation 2, where the reflection interface (shading red) is treated as a secondary source. The black curves represent the isochron of the travelttime field.

## 2. Adjoint-State Reflection Travelttime Tomography

In this section, we first formulate seismic tomography considering reflection arrivals as an optimization problem constrained by eikonal equations, and then employ the adjoint-state method to deduce the sensitivity kernels of the misfit function in relation to both velocity model and interface topography. Leveraging the derived sensitivity kernels, we employ an iterative optimization algorithm to update the velocity model and/or interface topography.

### 2.1. Forward Modeling and Optimization Problem

Consider a study region  $\Omega$  with a flatten surface and an undulating interface  $\Gamma$ , which can be expressed as  $\Omega = \{\mathbf{x} = (x, y, z) \mid x \in [x_{\min}, x_{\max}], y \in [y_{\min}, y_{\max}], z \in [0, d(x, y)]\}$ . Here  $x_{\min}, x_{\max}, y_{\min}$  and  $y_{\max}$  limit the range of the study region in two horizontal directions, and  $d(x, y)$  describes the geometric shapes of the interface  $\Gamma = \{\mathbf{x} \in \Omega \mid \mathbf{x} = (x, y, d(x, y))\}$ . Generally,  $d(x, y)$  needs to be second-order differentiable with respect to both variables. Considering earthquakes occurring within  $\Omega$  at location  $\mathbf{x}_{s,n}$  ( $n = 1, 2, \dots, N$ ) in the Cartesian coordinate system, we can calculate the seismic wave travelttime field about each source by solving the eikonal Equation 1 if the transmission medium is isotropic.

$$\begin{cases} \nabla T_n^I(\mathbf{x}) \cdot \nabla T_n^I(\mathbf{x}) = s^2(\mathbf{x}), \mathbf{x} \in \Omega \setminus \mathbf{x}_{s,n}, \\ T_n^I(\mathbf{x}_{s,n}) = 0. \end{cases} \quad (1)$$

Here  $s(\mathbf{x})$  describes the slowness at point  $\mathbf{x}$ , which is equal to the reciprocal of the velocity ( $s(\mathbf{x}) = 1/v(\mathbf{x})$ ). Following Rawlinson and Sambridge (2004a), we refer to  $T_n^I(\mathbf{x})$  as the incident travelttime field (Figure 1a). It gives the minimum travelttime from the source  $\mathbf{x}_{s,n}$  to any location  $\mathbf{x}$  in the study region  $\Omega$ , that is, the first arrival. According to Huygens' principle, we can treat the interface as a secondary source and calculate the arrival time of the reflection wave by solving the eikonal equation with corresponding boundary conditions

$$\begin{cases} \nabla T_n^R(\mathbf{x}) \cdot \nabla T_n^R(\mathbf{x}) = s^2(\mathbf{x}), \mathbf{x} \in \Omega \setminus \Gamma, \\ T_n^R(\mathbf{x}) = T_n^I(\mathbf{x}), \mathbf{x} \in \Gamma. \end{cases} \quad (2)$$

$T_n^R(\mathbf{x})$  is the reflected travelttime field (Figure 1b), giving the reflection arrival from the source  $\mathbf{x}_{s,n}$ , reflecting off the interface  $\Gamma$ , to any point  $\mathbf{x}$  within  $\Omega$ . To deal with the undulating interface  $\Gamma$ , we introduce the boundary-conforming grid (or body-fitted grid) (Thompson et al., 1985), which is based on the coordinate transformation from a rectangular computational (curvilinear) domain to an arbitrarily shaped physical (Cartesian) domain, as exemplified in Figure 2. Specifically, after the body-fitted grid is generated, grid points in physical domain  $\mathbf{x} = (x, y, z) \in \Omega$  and computational domain  $\xi = (\xi, \eta, \gamma) \in \hat{\Omega}$  have the following one-to-one mapping

$$\begin{cases} \xi = \xi(x, y, z) \\ \eta = \eta(x, y, z), \\ \gamma = \gamma(x, y, z) \end{cases} \quad \begin{cases} x = x(\xi, \eta, \gamma) \\ y = y(\xi, \eta, \gamma), \\ z = z(\xi, \eta, \gamma) \end{cases} \quad (3)$$

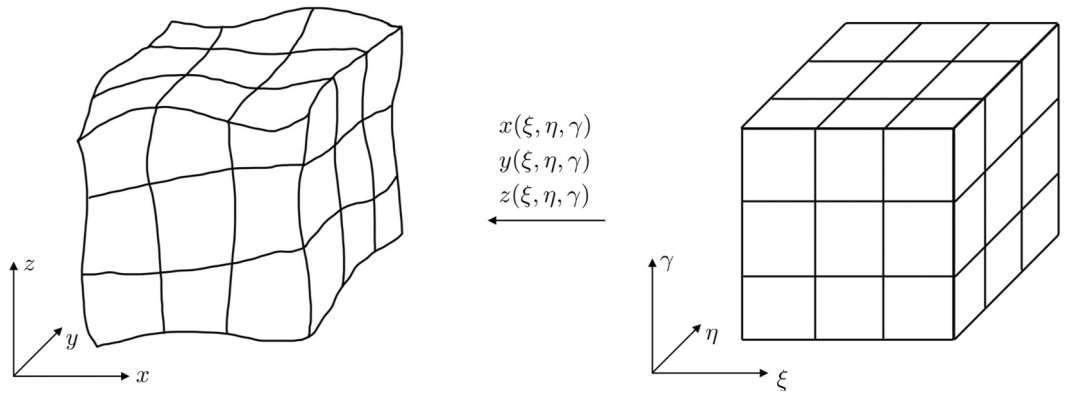


**Figure 2.** Mapping between the irregular physical domain and the regular computational domain.

We denote this mapping as  $\mathcal{G}$ , representing that  $\mathcal{G}(\mathbf{x}) = \xi$ , and  $\mathcal{G}^{-1}(\xi) = \mathbf{x}$ . By employing this, the undulating interface  $\Gamma \in \Omega$  can be converted into a flattened interface  $\hat{\Gamma} = \{\xi \in \hat{\Omega} \mid \mathcal{G}^{-1}(\xi) \in \Gamma\}$  in the computational domain  $\hat{\Omega} = \{\xi \mid \mathcal{G}^{-1}(\xi) \in \Omega\}$ , and the interface topography is encoded in parameters determined by the coordinate transformation. Consequently, the original isotropic eikonal equation is equivalently transformed into an interface-dependant anisotropic eikonal equation within a rectangular region. Specifically, we can reformulate the eikonal equation in curvilinear coordinates by chain rules

$$(T_\xi \xi_x + T_\eta \eta_x + T_\gamma \gamma_x)^2 + (T_\xi \xi_y + T_\eta \eta_y + T_\gamma \gamma_y)^2 + (T_\xi \xi_z + T_\eta \eta_z + T_\gamma \gamma_z)^2 = s^2. \quad (4)$$

A more compact form of Equation 4 is

$$\nabla T(\xi)' M_\Gamma \nabla T(\xi) = s(\xi)^2. \quad (5)$$

$\nabla T' = (T_\xi, T_\eta, T_\gamma)$  is the transpose of the gradient vector.  $M_\Gamma$  is an anisotropic parameter matrix, determined by the coordinate transformation, that is, by the interface  $\Gamma$ . In detail,

$$M_\Gamma = \begin{bmatrix} A & D & E \\ D & B & F \\ E & F & C \end{bmatrix} = \begin{bmatrix} \xi_x^2 + \xi_y^2 + \xi_z^2 & \xi_x \eta_x + \xi_y \eta_y + \xi_z \eta_z & \xi_x \gamma_x + \xi_y \gamma_y + \xi_z \gamma_z \\ \xi_x \eta_x + \xi_y \eta_y + \xi_z \eta_z & \eta_x^2 + \eta_y^2 + \eta_z^2 & \eta_x \gamma_x + \eta_y \gamma_y + \eta_z \gamma_z \\ \xi_x \gamma_x + \xi_y \gamma_y + \xi_z \gamma_z & \eta_x \gamma_x + \eta_y \gamma_y + \eta_z \gamma_z & \gamma_x^2 + \gamma_y^2 + \gamma_z^2 \end{bmatrix}, \quad (6)$$

Text S1 in Supporting Information S1 gives a detailed derivation of how to calculate the elements in  $M_\Gamma$ .

For imaging deep structures and/or reflectors, reflection waves offer unparalleled advantages over direct waves due to their distinctive propagation paths. The objective is to determine the most suitable slowness model and/or interface topography to minimize the discrepancy between observed and synthetic reflection arrivals. Consequently, it is reasonable to consider the optimization problem of the following form

$$\min_{s, \Gamma} \chi(s, \Gamma) = \sum_{n=1}^{N_s} \sum_{m=1}^{N_r} \frac{w_{n,m}^R}{2} (T_n^R(\hat{\mathbf{x}}_{r,m}) - t_{n,m}^{R,obs})^2, \quad (7a)$$

$$\text{s.t. } \begin{cases} (\nabla T_n^I(\xi))' M_\Gamma (\nabla T_n^I(\xi)) = s^2(\xi), \xi \in \hat{\Omega} \setminus \hat{\Gamma}_{s,n}, \\ T_n^I(\hat{\mathbf{x}}_{s,n}) = 0. \end{cases} \quad (7b)$$

$$\begin{cases} (\nabla T_n^R(\xi))' M_\Gamma (\nabla T_n^R(\xi)) = s^2(\xi), \xi \in \hat{\Omega} \setminus \hat{\Gamma}, \\ T_n^R(\xi) = T_n^I(\xi), \xi \in \hat{\Gamma}. \end{cases} \quad (7c)$$

Here,  $t_{n,m}^{R,obs}$  denotes the observed reflection arrival originating from the  $n$ th source  $\mathbf{x}_{s,n}$  ( $n = 1, 2, \dots, N_s$ ) and recorded by the  $m$ th receiver  $\mathbf{x}_{r,m}$  ( $m = 1, 2, \dots, N_r$ ) in the physical domain  $\Omega$ .  $\hat{\mathbf{x}}_{s,n} = \mathcal{G}(\mathbf{x}_{s,n})$  and  $\hat{\mathbf{x}}_{r,m} = \mathcal{G}(\mathbf{x}_{r,m})$  represent positions of the corresponding source and receiver, respectively, in the computational domain  $\hat{\Omega}$ . Similarly,  $\hat{\Gamma}$  represents a flat interface in the computational domain.  $w_{n,m}^R$  is the weight coefficient that indicates the reliability of observed data. The misfit function  $\chi(s, \Gamma)$  measures the distance between the observed data and synthetic data, where the synthetic reflection arrivals can be extracted from the traveltime field  $T_n^R(\xi)$ , which is determined by solving Equations 7b and 7c in the computational domain. Note that Equations 1 and 2 and Equations 7b and 7c are equivalent in describing the propagation of reflection waves, except that one is in the physical domain  $\Omega$  and the other is in the computational domain  $\hat{\Omega}$ . In the rest of this article, all calculations and derivations are performed in the computational domain unless otherwise specified. To solve this optimization problem, a fundamental step involves calculating the derivatives with respect to  $s(\xi)$  and  $\Gamma$ , which allows for the utilization of a gradient-based method to iteratively search for the optimal model.

## 2.2. The Fréchet Gradient About Slowness

In this section, we employ the adjoint-state method to derive the Fréchet derivative of the misfit function  $\chi$  with respect to the slowness model  $s$ , which enables us to estimate the Fréchet derivatives at a cost comparable to forward-modeling simulations (Lions & Magenes, 2012; Plessix, 2006).

We assign a small perturbation  $\delta s(\xi)$  to the slowness model, which causes perturbation of incident traveltime field  $\delta T_n^I(\xi)$  and reflected traveltime field  $\delta T_n^R(\xi)$ . Accordingly, the perturbated eikonal equation writes

$$\begin{cases} (\nabla(T_n^I(\xi) + \delta T_n^I(\xi)))^t M_\Gamma \nabla(T_n^I(\xi) + \delta T_n^I(\xi)) = (s(\xi) + \delta s(\xi))^2, \xi \in \hat{\Omega} \setminus \hat{\mathbf{x}}_{s,n}, \\ T_n^I(\hat{\mathbf{x}}_{s,n}) + \delta T_n^I(\hat{\mathbf{x}}_{s,n}) = 0. \end{cases} \quad (8)$$

$$\begin{cases} (\nabla(T_n^R(\xi) + \delta T_n^R(\xi)))^t M_\Gamma \nabla(T_n^R(\xi) + \delta T_n^R(\xi)) = (s(\xi) + \delta s(\xi))^2, \xi \in \hat{\Omega} \setminus \hat{\Gamma}, \\ T_n^R(\xi) + \delta T_n^R(\xi) = T_n^I(\xi) + \delta T_n^I(\xi), \xi \in \hat{\Gamma}. \end{cases} \quad (9)$$

Subtracting Equations 7b and 7c from Equations 8 and 9, ignoring second and higher order terms, we obtain

$$\begin{cases} (\nabla T_n^I(\xi))^t M_\Gamma \nabla \delta T_n^I(\xi) = s(\xi) \delta s(\xi), \xi \in \hat{\Omega} \setminus \hat{\mathbf{x}}_{s,n}, \\ \delta T_n^I(\hat{\mathbf{x}}_{s,n}) = 0. \end{cases} \quad (10)$$

$$\begin{cases} (\nabla T_n^R(\xi))^t M_\Gamma \nabla \delta T_n^R(\xi) = s(\xi) \delta s(\xi), \xi \in \hat{\Omega} \setminus \hat{\Gamma}, \\ \delta T_n^R(\xi) = \delta T_n^I(\xi), \xi \in \hat{\Gamma}. \end{cases} \quad (11)$$

Multiply a test function  $P_n^I(\xi)$  on both sides of Equation 10, and integrate it on  $\hat{\Omega}$ . Based on integration by parts and the divergence theorem, the left-hand side writes

$$\begin{aligned} L_n^I &= \int_{\hat{\Omega}} P_n^I (\nabla T_n^I)^t M_\Gamma \nabla \delta T_n^I d\xi = \int_{\hat{\Omega}} \nabla \cdot (P_n^I (\nabla T_n^I)^t M_\Gamma \delta T_n^I) d\xi - \int_{\hat{\Omega}} \delta T_n^I \nabla \cdot (P_n^I (\nabla T_n^I)^t M_\Gamma) d\xi \\ &= \int_{\partial \hat{\Omega}} \mathbf{n} \cdot (P_n^I (\nabla T_n^I)^t M_\Gamma \delta T_n^I) d\sigma + \int_{\hat{\Omega}} \delta T_n^I \nabla \cdot (P_n^I (-\nabla T_n^I)^t M_\Gamma) d\xi \triangleq L_n^{I_1} + L_n^{I_2}. \end{aligned} \quad (12)$$

Here  $\mathbf{n}$  represents the outward normal vector of the boundary  $\partial \hat{\Omega}$ , and the symbol  $\triangleq$  denotes that we define the first and second term of  $L_n^I$  as  $L_n^{I_1}$  and  $L_n^{I_2}$ , respectively. Similarly, for the reflected traveltime field, considering a test function  $P_n^R(\xi)$  and combining Equation 11, we have

$$L_n^R = \int_{\hat{\Omega}} \mathbf{n} \cdot \left( P_n^R (\nabla T_n^R)^t M_\Gamma \delta T_n^R \right) d\sigma + \int_{\hat{\Omega}} \delta T_n^R \nabla \cdot \left( P_n^R (-\nabla T_n^R)^t M_\Gamma \right) d\xi \triangleq L_n^{R_1} + L_n^{R_2}. \quad (13)$$

Let  $\partial\hat{\Omega} = (\partial\hat{\Omega} \setminus \hat{\Gamma}) \cup \hat{\Gamma}$ , and assume that  $P_n^I(\xi)$ ,  $P_n^R(\xi)$  satisfy the following adjoint equations

$$\begin{cases} \nabla \cdot \left( P_n^R(\xi) (-\nabla T_n^R(\xi))^t M_\Gamma \right) = \sum_{m=1}^{N_r} w_{n,m}^R (T_n^R(\xi) - t_{n,m}^{R,obs}) \delta(\xi - \hat{x}_{r,m}), \\ P_n^R(\xi) = 0, \xi \in \partial\hat{\Omega} \setminus \hat{\Gamma}. \end{cases} \quad (14)$$

$$\begin{cases} \nabla \cdot \left( P_n^I(\xi) (-\nabla T_n^I(\xi))^t M_\Gamma \right) = 0, \\ P_n^I(\xi) = 0, \xi \in \partial\hat{\Omega} \setminus \hat{\Gamma}, \\ P_n^I(\xi) = P_n^R(\xi), \xi \in \hat{\Gamma}. \end{cases} \quad (15)$$

Note that  $\delta(\xi - \hat{x}_{r,m})$  in Equation 14 is the Dirac delta function. By substituting Equations 14 and 15 into  $L_n^{R_2}$  and  $L_n^{I_2}$ , we can obtain that

$$L_n^{R_2} + L_n^{I_2} = \int_{\hat{\Omega}} \delta T_n^R \sum_{m=1}^{N_r} w_{n,m}^R (T_n^R(\xi) - t_{n,m}^{R,obs}) \delta(\xi - \hat{x}_{r,m}) d\xi = \delta T_n^R(\hat{x}_{r,m}) \sum_{m=1}^{N_r} w_{n,m}^R (T_n^R(\hat{x}_{r,m}) - t_{n,m}^{R,obs}). \quad (16)$$

Similarly,

$$\begin{aligned} L_n^{R_1} + L_n^{I_1} &= \int_{\hat{\Omega}} \mathbf{n} \cdot \left( P_n^R (\nabla T_n^R)^t M_\Gamma \delta T_n^R \right) d\sigma + \int_{\hat{\Omega}} \mathbf{n} \cdot \left( P_n^I (\nabla T_n^I)^t M_\Gamma \delta T_n^I \right) d\sigma \\ &= \int_{\hat{\Gamma}} \mathbf{n} \cdot \left( (\nabla T_n^R + \nabla T_n^I)^t \right) M_\Gamma \delta T_n^I P_n^I d\sigma. \end{aligned} \quad (17)$$

By Snell's Law, on the interface  $\Gamma$ , we have

$$\mathbf{n} \cdot (\nabla T_n^I)^t = -\mathbf{n} \cdot (\nabla T_n^R)^t, \quad (18)$$

which indicates that  $L_n^{R_1} + L_n^{I_1} = 0$ . In this way,

$$L_n = L_n^I + L_n^R = L_n^{I_1} + L_n^{I_2} + L_n^{R_1} + L_n^{R_2} = \delta T_n^R(\hat{x}_{r,m}) \sum_{m=1}^{N_r} w_{n,m}^R (T_n^R(\hat{x}_{r,m}) - t_{n,m}^{R,obs}). \quad (19)$$

Considering the right-hand side terms of Equations 10 and 11, it is easy to obtain

$$R_n = \int_{\hat{\Omega}} (P_n^I(\xi) + P_n^R(\xi)) s(\xi) \delta s(\xi) d\xi. \quad (20)$$

On the other hand, the perturbation of misfit function  $\delta\chi$  can be formed by ignoring the second and higher-order terms

$$\begin{aligned} \delta\chi &= \chi(s + \delta s) - \chi(s) = \sum_{n=1}^{N_s} \sum_{m=1}^{N_r} w_{n,m}^R (T_n^R(\hat{x}_{r,m}) - t_{n,m}^{R,obs}) \delta T_n^R(\hat{x}_{r,m}) \\ &= \sum_{n=1}^{N_s} L_n = \sum_{n=1}^{N_s} R_n = \int_{\hat{\Omega}} \sum_{n=1}^{N_s} K_n^s(\xi) \frac{\delta s(\xi)}{s(\xi)} d\xi = \int_{\hat{\Omega}} K_s(\xi) \frac{\delta s(\xi)}{s(\xi)} d\xi, \end{aligned} \quad (21)$$

where

$$K_s(\xi) = \sum_{n=1}^{N_s} K_n^s(\xi) = \sum_{n=1}^{N_s} (P_n^I(\xi) + P_n^R(\xi)) s^2(\xi). \quad (22)$$

Equation 21 establishes an approximate linear relationship between the perturbation of the misfit function  $\delta\chi$  and the perturbation of the slowness model  $\delta s(\xi)$ .  $K_s(\xi)$  (named misfit kernel) is the Fréchet derivative of the misfit function with respect to slowness. By examining Equation 22, we can intuitively find that  $K_s(\xi)$  is a linear combination of  $K_n^s(\xi)$  (named event kernel). In particular, the event kernel determined by one source-receiver pair is called an individual kernel, which provides information about the slowness structure along the reflection wave path of this source-receiver pair. For each source, only a two-stage eikonal equation of Equations 7b and 7c for traveltime field and a two-stage adjoint equation of Equations 14 and 15 for adjoint field should be solved, implying that the computational cost is proportional to the number of sources ( $N_s$ ) and independent of the number of receivers ( $N_r$ ).

### 2.3. The Fréchet Gradient About Interface Topography

In this section, we use the adjoint-state method to derive the Fréchet derivative of the misfit function  $\chi$  with respect to the interface  $\Gamma$ . That is, we need to delineate an approximately linear relationship between the misfit function perturbation  $\delta\chi$  and the interface topography perturbation  $\delta d$ , considering that the interface  $\Gamma$  is completely characterized by parameter  $d$ . As explicated in Section 2.1, a coordinate transformation was introduced to convert the irregular interface in the physical domain into a flattened interface in the computational domain, where the interface information is encoded in the anisotropic matrix  $M_\Gamma$  determined by the coordinate transformation. Therefore, the sensitivity kernel can be explicitly formulated by considering the quantitative relationship between the interface  $\Gamma$  and the anisotropic matrix  $M_\Gamma$ .

For simplicity of derivation, we choose a simple linear stretch to complete the mapping between the physical domain and the computational domain (Fornberg, 1988; Tessmer et al., 1992). That is, in three-dimensional space, we consider the following coordinate transformation relationship

$$\begin{cases} x(\xi, \eta, \gamma) = \xi, \\ y(\xi, \eta, \gamma) = \eta, \\ z(\xi, \eta, \gamma) = \frac{d(\xi, \eta)}{\gamma_{\max}} \gamma. \end{cases} \quad (23)$$

$d(\xi, \eta)$  defines the interface topography, and the rectangular  $(\xi, \eta, \gamma)$ -grid is defined by  $[\xi_{\min}, \xi_{\max}] \times [\eta_{\min}, \eta_{\max}] \times [0, \gamma_{\max}]$ . It should be noted that  $\gamma_{\max}$  are subjectively selected. Generally, we can set  $\gamma_{\max}$  close to  $d(\xi, \eta)$  (such as the average depth of the interface  $\Gamma$ ). Under such a mapping, we can determine the anisotropic parameter matrix  $M_\Gamma$  according to Equation 6

$$M_\Gamma = \begin{bmatrix} A & D & E \\ D & B & F \\ E & F & C \end{bmatrix} = \begin{bmatrix} 1 & 0 & -\frac{\gamma d_\xi}{d} \\ 0 & 1 & -\frac{\gamma d_\eta}{d} \\ -\frac{\gamma d_\xi}{d} & -\frac{\gamma d_\eta}{d} & \frac{\gamma^2(d_\xi^2 + d_\eta^2) + \gamma_{\max}^2}{d^2} \end{bmatrix}. \quad (24)$$

We assign a small perturbation  $\delta d(\xi, \eta)$  to the interface  $d(\xi, \eta)$ , which causes the perturbation of coordinate transformation in the vertical direction

$$z(\xi, \eta, \gamma) = \frac{d(\xi, \eta) + \delta d(\xi, \eta)}{\gamma_{\max}} \gamma. \quad (25)$$

Further, the perturbed anisotropic matrix  $M_\Gamma + \delta M_\Gamma$  is determined as

$$\begin{aligned}
 M_\Gamma + \delta M_\Gamma &= M_\Gamma + \begin{bmatrix} \delta A & \delta D & \delta E \\ \delta D & \delta B & \delta F \\ \delta E & \delta F & \delta C \end{bmatrix} \\
 &= \begin{bmatrix} 1 & 0 & -\frac{\gamma(d_\xi + \delta d_\xi)}{d + \delta d} \\ 0 & 1 & -\frac{\gamma(d_\eta + \delta d_\eta)}{d + \delta d} \\ -\frac{\gamma(d_\xi + \delta d_\xi)}{d + \delta d} & -\frac{\gamma(d_\eta + \delta d_\eta)}{d + \delta d} & \frac{\gamma^2((d_\xi + \delta d_\xi)^2 + (d_\eta + \delta d_\eta)^2) + \gamma_{\max}^2}{(d + \delta d)^2} \end{bmatrix}. \quad (26)
 \end{aligned}$$

Plugging Equation 24 into Equation 26, we can directly know that

$$\delta A = 0, \delta B = 0, \delta D = 0. \quad (27)$$

Keeping only the first-order term, we have

$$\delta E = -\frac{\gamma(d_\xi + \delta d_\xi)}{d + \delta d} + \frac{\gamma d_\xi}{d} = -\gamma \frac{\partial \ln(d + \delta d)}{\partial \xi} + \gamma \frac{\partial \ln d}{\partial \xi} = -\gamma \frac{\partial}{\partial \xi} \ln \left( 1 + \frac{\delta d}{d} \right) = -\gamma \frac{\partial}{\partial \xi} \frac{\delta d}{d}, \quad (28)$$

Similarly,

$$\delta F = -\gamma \frac{\partial}{\partial \eta} \frac{\delta d}{d}. \quad (29)$$

$$\begin{aligned}
 \delta C &= \left( \gamma \frac{\partial \ln(d + \delta d)}{\partial \xi} \right)^2 + \left( \gamma \frac{\partial \ln(d + \delta d)}{\partial \eta} \right)^2 + \frac{\gamma_{\max}^2}{(d + \delta d)^2} - \left( \gamma \frac{\partial \ln d}{\partial \xi} \right)^2 - \left( \gamma \frac{\partial \ln d}{\partial \eta} \right)^2 - \frac{\gamma_{\max}^2}{d^2} \\
 &= 2\gamma^2 \frac{d_\xi}{d} \frac{\partial}{\partial \xi} \frac{\delta d}{d} + 2\gamma^2 \frac{d_\eta}{d} \frac{\partial}{\partial \eta} \frac{\delta d}{d} - 2 \frac{\gamma_{\max}^2}{d^2} \frac{\delta d}{d}.
 \end{aligned} \quad (30)$$

Similar to the derivation in Section 2.2, the perturbation of the anisotropic matrix  $\delta M_\Gamma$  caused by the perturbation of the interface topography  $\delta d$  results in corresponding perturbations in the incident traveltime field  $\delta T_n^I(\xi)$  and the reflected traveltime field  $\delta T_n^R(\xi)$ , which satisfy the perturbed eikonal equations below

$$\begin{cases} (\nabla(T_n^I(\xi) + \delta T_n^I(\xi)))^t (M_\Gamma + \delta M_\Gamma) \nabla(T_n^I(\xi) + \delta T_n^I(\xi)) = s^2(\xi), \xi \in \hat{\Omega} \setminus \hat{x}_{s,n}, \\ T_n^I(\hat{x}_{s,n}) + \delta T_n^I(\hat{x}_{s,n}) = 0. \end{cases} \quad (31)$$

$$\begin{cases} (\nabla(T_n^R(\xi) + \delta T_n^R(\xi)))^t (M_\Gamma + \delta M_\Gamma) \nabla(T_n^R(\xi) + \delta T_n^R(\xi)) = s^2(\xi), \xi \in \hat{\Omega} \setminus \hat{\Gamma}, \\ T_n^R(\xi) + \delta T_n^R(\xi) = T_n^I(\xi) + \delta T_n^I(\xi), \xi \in \hat{\Gamma}. \end{cases} \quad (32)$$

Subtracting Equations 7b and 7c from Equations 31 and 32, and ignoring second and higher order terms, we obtain

$$\begin{cases} (\nabla T_n^I(\xi))^t M_\Gamma \nabla \delta T_n^I(\xi) = -\frac{1}{2} (\nabla T_n^I(\xi))^t \delta M_\Gamma \nabla T_n^I(\xi), \xi \in \hat{\Omega} \setminus \hat{x}_{s,n}, \\ \delta T_n^I(\hat{x}_{s,n}) = 0. \end{cases} \quad (33)$$

$$\begin{cases} (\nabla T_n^R(\xi))^t M_\Gamma \nabla \delta T_n^R(\xi) = -\frac{1}{2} (\nabla T_n^R(\xi))^t \delta M_\Gamma \nabla T_n^R(\xi), \xi \in \hat{\Omega} \setminus \hat{\Gamma}, \\ \delta T_n^R(\xi) = \delta T_n^I(\xi), \xi \in \hat{\Gamma}. \end{cases} \quad (34)$$

We also multiply the test functions  $P_n^I(\xi)$  and  $P_n^R(\xi)$  on both sides of Equations 33 and 34 respectively, and integrate them on  $\hat{\Omega}$ . Note that the left-hand part is exactly the same as Equations 10 and 11, so the results remain consistent if  $P_n^R(\xi)$  and  $P_n^I(\xi)$  satisfy the adjoint Equations 14 and 15. Specifically,

$$L_n^I = \int_{\hat{\Omega}} P_n^I (\nabla T_n^I)^t M_\Gamma \nabla \delta T_n^I d\xi + \int_{\hat{\Omega}} P_n^R (\nabla T_n^R)^t M_\Gamma \nabla \delta T_n^R d\xi = \sum_{m=1}^N w_{n,m}^R (T_n^R(\hat{x}_{r,m}) - t_{n,m}^{R,obs}) \delta T_n^R(\hat{x}_{r,m}). \quad (35)$$

For the right-hand part, we take Equation 33 as an example

$$R_n^I = \int_{\hat{\Omega}} P_n^I \left( -\frac{1}{2} (\nabla T_n^I)^t \delta M_\Gamma \nabla T_n^I \right) d\xi = \int_{\hat{\Omega}} P_n^I \left( -\delta E \partial_\xi T_n^I \partial_\gamma T_n^I - \delta F \partial_\eta T_n^I \partial_\gamma T_n^I - \frac{\delta C}{2} (\partial_\gamma T_n^I)^2 \right) d\xi. \quad (36)$$

The three integral terms in Equation 36 will be processed sequentially. Substituting into Equation 28, using Green's theorem and integration by parts, the first term can be written as

$$\begin{aligned} \int_{\hat{\Omega}} P_n^I (-\delta E \partial_\xi T_n^I \partial_\gamma T_n^I) d\xi &= \int_{\xi_{\min}}^{\xi_{\max}} \int_{\eta_{\min}}^{\eta_{\max}} \frac{\partial}{\partial \xi} \frac{\delta d}{d} \left( \int_0^{\gamma_{\max}} \gamma P_n^I \partial_\xi T_n^I \partial_\gamma T_n^I d\gamma \right) d\eta d\xi \\ &= \oint_{\partial Q} \frac{\delta d}{d} \left( \int_0^{\gamma_{\max}} \gamma P_n^I \partial_\xi T_n^I \partial_\gamma T_n^I d\gamma \right) d\eta - \iint_Q \partial_\xi \left( \int_0^{\gamma_{\max}} \gamma P_n^I \partial_\xi T_n^I \partial_\gamma T_n^I d\gamma \right) \frac{\delta d}{d} d\xi d\eta, \end{aligned} \quad (37)$$

where  $Q = [\xi_{\min}, \xi_{\max}] \times [\eta_{\min}, \eta_{\max}]$  is a two-dimensional plane with boundary  $\partial Q$ . If we further assume that  $\delta d|_{\partial Q} = 0$ , then the first term of Equation 37 vanishes, leading that

$$\int_{\hat{\Omega}} P_n^I (-\delta E \partial_\xi T_n^I \partial_\gamma T_n^I) d\xi = -\iint_Q \partial_\xi \left( \int_0^{\gamma_{\max}} \gamma P_n^I \partial_\xi T_n^I \partial_\gamma T_n^I d\gamma \right) \frac{\delta d}{d} d\xi d\eta. \quad (38)$$

The second term of Equation 36 can be treated in the same way and we get

$$\int_{\hat{\Omega}} P_n^I (-\delta F \partial_\eta T_n^I \partial_\gamma T_n^I) d\xi = -\iint_Q \partial_\eta \left( \int_0^{\gamma_{\max}} \gamma P_n^I \partial_\eta T_n^I \partial_\gamma T_n^I d\gamma \right) \frac{\delta d}{d} d\xi d\eta, \quad (39)$$

while the last integral term becomes

$$\begin{aligned} \int_{\hat{\Omega}} P_n^I \left( -\frac{\delta C}{2} (\partial_\gamma T_n^I)^2 \right) d\xi &= \int_{\hat{\Omega}} P_n^I \left( -\gamma^2 \frac{d_\xi}{d} \frac{\partial}{\partial \xi} \frac{\delta d}{d} - \gamma^2 \frac{d_\eta}{d} \frac{\partial}{\partial \eta} \frac{\delta d}{d} + \frac{\gamma_{\max}^2}{d^2} \frac{\delta d}{d} \right) (\partial_\gamma T_n^I)^2 d\xi \\ &= \iint_Q \left( \partial_\xi \left( \int_0^{\gamma_{\max}} \gamma^2 P_n^I (\partial_\gamma T_n^I)^2 d\gamma \frac{d_\xi}{d} \right) + \partial_\eta \left( \int_0^{\gamma_{\max}} \gamma^2 P_n^I (\partial_\gamma T_n^I)^2 d\gamma \frac{d_\eta}{d} \right) + \right. \\ &\quad \left. \int_0^{\gamma_{\max}} P_n^I (\partial_\gamma T_n^I)^2 \frac{\gamma_{\max}^2}{d^2} d\gamma \right) \frac{\delta d}{d} d\xi d\eta. \end{aligned} \quad (40)$$

By combining Equations 36–40, we can obtain that

$$R_n^I = \iint_Q K_n^I \frac{\delta d}{d} d\xi d\eta, \quad (41)$$

where

$$\begin{aligned} K_n^I &= -\partial_\xi \left( \int_0^{\gamma_{\max}} \gamma P_n^I \partial_\xi T_n^I \partial_\gamma T_n^I d\gamma \right) - \partial_\eta \left( \int_0^{\gamma_{\max}} \gamma P_n^I \partial_\eta T_n^I \partial_\gamma T_n^I d\gamma \right) \\ &+ \partial_\xi \left( \int_0^{\gamma_{\max}} \gamma^2 P_n^I (\partial_\gamma T_n^I)^2 d\gamma \frac{d_\xi}{d} \right) + \partial_\eta \left( \int_0^{\gamma_{\max}} \gamma^2 P_n^I (\partial_\gamma T_n^I)^2 d\gamma \frac{d_\eta}{d} \right) + \int_0^{\gamma_{\max}} P_n^I (\partial_\gamma T_n^I)^2 \frac{\gamma_{\max}^2}{d^2} d\gamma. \end{aligned} \quad (42)$$

For the reflection part in Equation 34, repeating the above derivation and replacing the superscript “ $I$ ” with “ $R$ ” yields

$$R_n^R = \iint_Q K_n^R \frac{\delta d}{d} d\xi d\eta, \quad (43)$$

where

$$\begin{aligned} K_n^R &= -\partial_\xi \left( \int_0^{\gamma_{\max}} \gamma P_n^R \partial_\xi T_n^R \partial_\gamma T_n^R d\gamma \right) - \partial_\eta \left( \int_0^{\gamma_{\max}} \gamma P_n^R \partial_\eta T_n^R \partial_\gamma T_n^R d\gamma \right) \\ &+ \partial_\xi \left( \int_0^{\gamma_{\max}} \gamma^2 P_n^R (\partial_\gamma T_n^R)^2 d\gamma \frac{d_\xi}{d} \right) + \partial_\eta \left( \int_0^{\gamma_{\max}} \gamma^2 P_n^R (\partial_\gamma T_n^R)^2 d\gamma \frac{d_\eta}{d} \right) + \int_0^{\gamma_{\max}} P_n^R (\partial_\gamma T_n^R)^2 \frac{\gamma_{\max}^2}{d^2} d\gamma. \end{aligned} \quad (44)$$

Finally, the integral term on the right side can be expressed as follows

$$\begin{aligned} R_n &= \int_{\Omega} P_n^I \left( -\frac{1}{2} (\nabla T_n^I)^t \delta M \nabla T_n^I \right) d\xi + \int_{\Omega} P_n^R \left( -\frac{1}{2} (\nabla T_n^R)^t \delta M \nabla T_n^R \right) d\xi \\ &= R_n^I + R_n^R = \iint_Q (K_n^I + K_n^R) \frac{\delta d}{d} d\xi d\eta. \end{aligned} \quad (45)$$

On the other hand, we consider the perturbation of the misfit function  $\delta\chi$  caused by the interface perturbation

$$\delta\chi = \sum_{n=1}^{N_s} \sum_{m=1}^{N_r} w_{n,m}^R (T_n^R(\hat{x}_{r,m}) - t_{n,m}^{R,obs}) \delta T_n^R(\hat{x}_{r,m}) = \sum_{n=1}^{N_s} L_n = \sum_{n=1}^{N_s} R_n = \iint_Q K_f \frac{\delta d}{d} d\xi d\eta, \quad (46)$$

where

$$K_f = \sum_{n=1}^{N_s} K_n^f = \sum_{n=1}^{N_s} (K_n^I + K_n^R). \quad (47)$$

Equation 46 constructs a linear relationship between the misfit function perturbation  $\delta\chi$  and the interface topography perturbation  $\delta d$ .  $K_f$  is the sensitivity kernel of the misfit function with respect to the interface, which is explicitly determined by the traveltime field  $T_n^I$ ,  $T_n^R$  and the adjoint field  $P_n^I$ ,  $P_n^R$  about each source.

## 2.4. Inversion Procedures

After obtaining the sensitivity kernel about slowness or interface topography, the multiple-grid model parameterization (Tong et al., 2019) and step size-controlled gradient descent method (Tong, 2021a) are considered to iteratively update the slowness model or interface topography until the misfit function stabilizes or converges. The utilization of the multiple-grid method provides implicit smoothing regularization on sensitivity kernels, thereby effectively mitigating artificial anomalies caused by subjective inversion grid selection. Damping regularization is implemented through the step size-controlled gradient descent method. Specifically, we set the upper and lower bounds of parameter perturbation as  $\pm 2\%$  of the current model, and dynamically modulate the step size in response to the trajectory of the misfit function. In all subsequent synthetic tests and practical applications, these two methods are applied in the inversion. The optimization algorithms for slowness inversion, interface topography inversion, and joint inversion for both the slowness model and interface topography based on reflection arrivals are presented below.

We first consider the inversion of the slowness model (Algorithm 1). It is worth mentioning that our assumption includes complete knowledge of the interface  $\Gamma$ , implying that the anisotropic parameter matrix  $M_\Gamma$  is accurately determined by the coordinate transformation and will remain invariant throughout the iteration.

---

**Algorithm 1.** Slowness Model Inversion Procedure

---

**Input:**

The initial slowness model  $s_0(\xi)$   
The determined interface topography  $d(\xi, \eta)$   
Maximum iteration step  $L$

**Output:**

Final slowness model  $s_i(\xi)$

- 1: Determine  $M_\Gamma$  based on Equation 6 (or specifically, Equation 24)
- 2: Iteration step  $i = 0$
- 3: **repeat**
- 4:  $K_s = 0$
- 5: **for**  $n = 1, \dots, N_s$  **do**
- 6: Calculate the incident traveltime field  $T_n^I$  based on Equation 7b
- 7: Calculate the reflected traveltime field  $T_n^R$  based on Equation 7c
- 8: Calculate the reflected adjoint field  $P_n^R$  based on Equation 14
- 9: Calculate the incident adjoint field  $P_n^I$  based on Equation 15
- 10: Determine the slowness event kernel  $K_n^s$  based on Equation 22
- 11: Update the misfit kernel  $K_s = K_s + K_n^s$
- 12: **end for**
- 13: Calculate the misfit function  $\chi_i$  based on Equation 7a
- 14: Determine slowness model  $s_{i+1}(\xi)$  based on  $K_s$  considering the multiple-grid and step size-controlled gradient descent method
- 15:  $i = i + 1$
- 16: **until**  $i \geq L$

---

Similarly, Algorithm 2 presents the workflow for the inversion of interface topography. It is essential to emphasize that modifications to the interface topography will cause alterations to the coordinate transformation. Consequently, it becomes necessary to re-determine the anisotropic matrix  $M_\Gamma$  after each iteration, which distinguishes it from the slowness inversion procedures.

---

**Algorithm 2.** Interface Topography Inversion Procedure

---

**Input:**

The initial interface topography  $d_0(\xi, \eta)$   
The determined slowness model  $s(\xi)$   
Maximum iteration step  $L$

**Output:**

Final interface topography  $d_i(\xi, \eta)$

- 1: Iteration  $i = 0$
- 2: **repeat**
- 3: Determine  $M_\Gamma$  based on Equation 24
- 4:  $K_f = 0$
- 5: **for**  $n = 1, \dots, N_s$  **do**
- 6: Calculate the incident traveltime field  $T_n^I$  based on Equation 7b
- 7: Calculate the reflected traveltime field  $T_n^R$  based on Equation 7c
- 8: Calculate the reflected adjoint field  $P_n^R$  based on Equation 14
- 9: Calculate the incident adjoint field  $P_n^I$  based on Equation 15
- 10: Calculate the interface event kernel  $K_n^I$  and  $K_n^R$  based on Equations 42 and 44

---

```
11:    Update the misfit kernel  $K_f = K_f + K_n^I + +K_n^R$ 
12: end for
13: Calculate the misfit function  $\chi_i$  based on Equation 7a
14: Update interface topography  $d_{i+1}(\xi, \eta)$  based on  $K_f$  considering the multiple-
     grid and
     step size-controlled gradient descent method
15:  $i = i + 1$ 
16: until  $i \geq L$ 
```

The implementation of a joint inversion (Algorithm 3) for both slowness and interface topography can be straightforwardly achieved by integrating Algorithm 1 and Algorithm 2, as these two algorithms are based on independent sensitivity kernels. In the following numerical experiments, we update the slowness model and/or interface topography based on Algorithm 1–3 when reflection arrivals are considered.

---

**Algorithm 3.** Joint Inversion Procedure

---

**Input:**

The initial slowness model  $s_0(\xi)$   
The initial interface topography  $d_0(\xi, \eta)$   
Maximum iteration step  $L$

**Output:**

Final slowness model  $s_i(\xi)$   
Final interface topography  $d_i(\xi, \eta)$

```
1: Iteration  $i = 0$ 
2: repeat
3:   Determine  $M_T$  based on Equation 24
4:    $K_s = 0, K_f = 0$ 
5:   for  $n = 1, \dots, N_s$  do
6:     Calculate the incident traveltime field  $T_n^I$  based on Equation 7b
7:     Calculate the reflected traveltime field  $T_n^R$  based on Equation 7c
8:     Calculate the reflected adjoint field  $P_n^R$  based on Equation 14
9:     Calculate the incident adjoint field  $P_n^I$  based on Equation 15
10:    Determine the slowness event kernel  $K_n^S$  based on Equation 22
11:    Calculate the interface event kernel  $K_n^I$  and  $K_n^R$  based on Equations 42 and 44
12:    Update the slowness misfit kernel  $K_s = K_s + K_n^S$ 
13:    Update the interface misfit kernel  $K_f = K_f + K_n^I + +K_n^R$ 
14:   end for
15:   Calculate the misfit function  $\chi_i$  based on Equation 7a
16:   Determine slowness model  $s_{i+1}(\xi)$  based on  $K_s$  considering the multiple-grid and
     step size-controlled gradient descent method
17:   Update interface topography  $d_{i+1}(\xi, \eta)$  based on  $K_f$  considering the multiple-
     grid and step size-controlled gradient descent method
18:    $i = i + 1$ 
19: until  $i \geq L$ 
```

---

### 3. Numerical Experiments

Below we design several numerical experiments to exhibit the performance of the proposed method. In our numerical tests, both first arrivals and reflection arrivals are utilized for slowness inversion. One can refer to Tong (2021a, 2021b) for a detailed derivation of the adjoint-state traveltime tomography method based on first arrivals. Considering the linear superposition property of sensitivity kernels, it can be easily embedded into the slowness inversion algorithm.

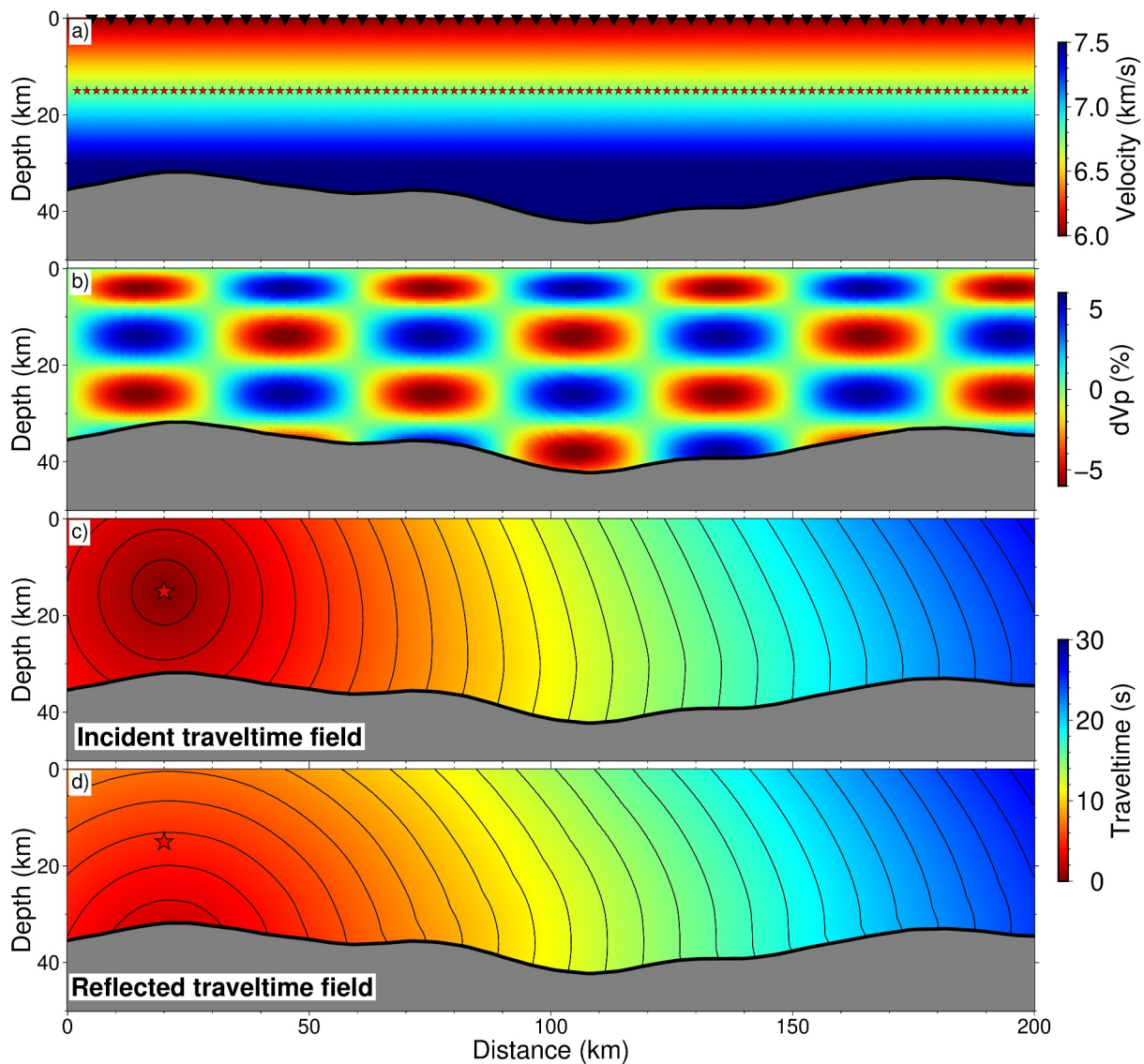


**Figure 3.** Settings for the 3D checkerboard test. Since the  $y$  direction is identical, only the cross-section with  $y = 5$  km is shown. The same applies to Figures 4–6. (a) Black inverted triangles on the surface mark the locations of receivers, and the red stars are sources. The initial velocity model is a linearly increasing velocity model, and the black line represents the interface topography. (b) The velocity anomaly perturbation added to the initial model. (c) The incident traveltime field excited by the source located at [20 km, 15 km]. The black curve represents the traveltime isochrone. (d) Reflected traveltime field excited by the same source.

### 3.1. Velocity Inversion

To elucidate the efficacy of reflection arrivals in constraining deep geological structures, we perform a checkerboard test for velocity inversion first. Consider an irregular bounded physical domain  $\Omega = \{x = (x, y, z) \mid x \in [0 \text{ km}, 200 \text{ km}], y \in [0 \text{ km}, 10 \text{ km}], z \in [0 \text{ km}, d(x, y)]\}$ .  $d(x, y)$  describes the topography of interface  $\Gamma$  (black curve in Figure 3). This interface is defined by a series of discrete nodes. The initial velocity model  $v_0$  (Figure 3a) is determined as

$$v_0(x, y, z) = \min(6.0 + 0.05z, 7.5), \quad (48)$$

which is identical along the  $y$  direction. The target velocity model  $v_t$  is constructed by introducing a velocity perturbation  $\Delta v$  (as depicted in Figure 3b) of up to  $\pm 6\%$  into the initial model  $v_0$ , that is,  $v_t = v_0(1 + \Delta v)$ , where

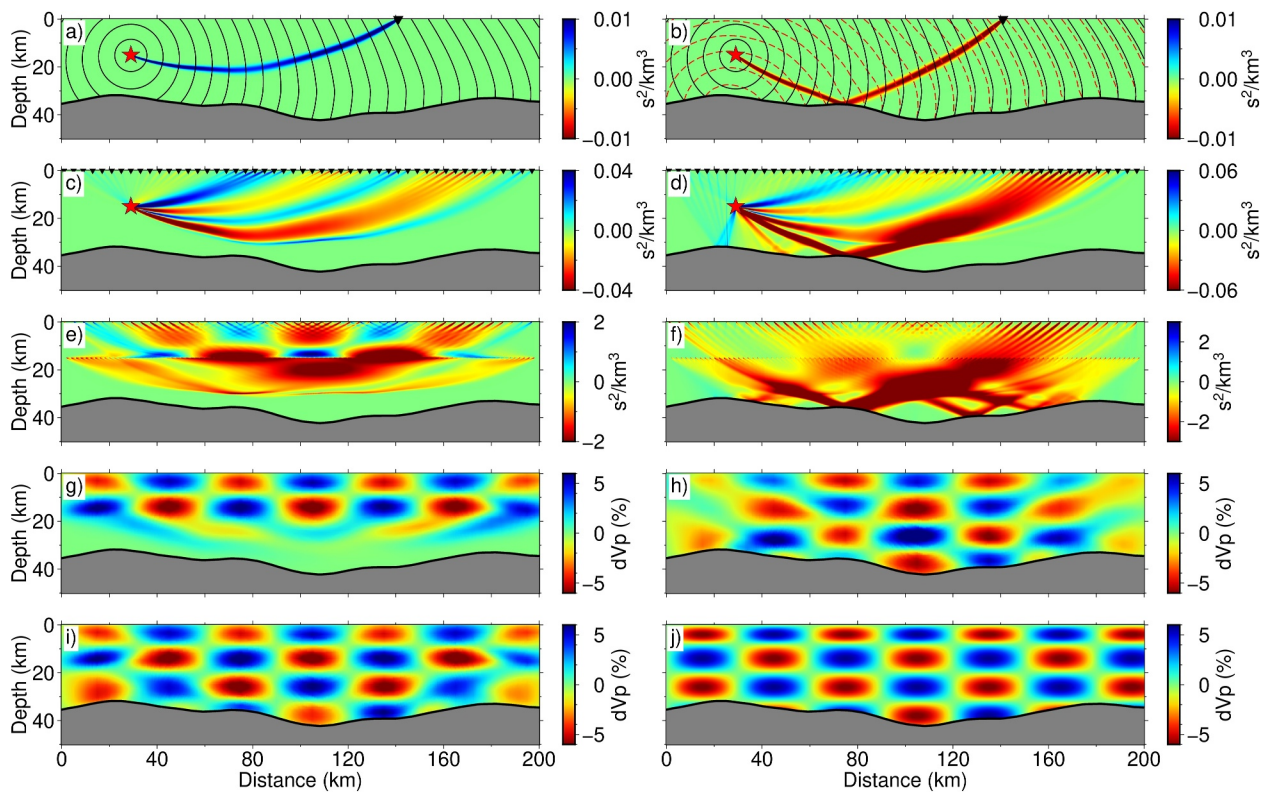


**Figure 4.** Inversion results for 3D checkerboard test at the profile  $y = 5$  km. (a) The individual kernel for first arrival calculated based on a specific source-receiver pair, one can refer to Tong (2021a) for a detailed introduction. (b) The individual kernel for reflection arrival calculated based on a specific source-receiver pair, which is obtained by numerically solving the adjoint Equations 14 and 15 considering fast sweeping method (Leung & Qian, 2006; Taillandier et al., 2009). (c) The event kernel for first arrivals based on a given source (red star). (d) The event kernel for reflection arrivals based on the same source. (e) The misfit kernel obtained based on the initial model, only first arrivals are considered. (f) The misfit kernel obtained based on the initial model, only reflection arrivals are considered. (g) Tomographic results using only first arrivals. (h) Tomographic results using only reflection arrivals. (i) Tomographic results for joint inversion of first arrivals and reflection arrivals. (j) Target velocity model.

$$\Delta v(x, y, z) = \begin{cases} -0.06 \sin\left(\frac{\pi}{30}x\right) \sin\left(\frac{\pi}{8}z\right), & z \leq 8, \\ 0.06 \sin\left(\frac{\pi}{30}x\right) \sin\left(\frac{\pi}{12}z - \frac{2}{3}\pi\right), & z > 8. \end{cases} \quad (49)$$

We simulated the “observed” first arrivals and reflection arrivals based on  $v_t$ , and initiated the inversion from  $v_0$ . The recovery of velocity anomaly blocks at different locations visually demonstrates whether the data can reconstruct the velocity anomaly at the corresponding scale.

We uniformly deployed 50 receivers on the free surface and 99 sources at a depth of 15 km, with 2 km apart (Figure 3a). All sources and stations lie on  $y = 5$  km, as do the profiles shown below. Here we employed the multiplicative factorization-based fast sweeping method (J. Chen et al., 2023; Fomel et al., 2009; Kao et al., 2004; Luo & Qian, 2011) to numerically solve the forward eikonal equation at the discretized grid points. This method demonstrates robust performance in addressing the singularity associated with point sources. Figures 3c and 3d illustrate the incident traveltime field and the reflected traveltime field, respectively. These traveltime fields yield synthetic first arrivals and reflection arrivals for all receivers.

We present the tomographic results considering first arrivals exclusively, reflection arrivals exclusively, and the joint inversion (Figures 4g–4i). Figures 4a–4f illustrate examples of individual kernels, event kernels, and misfit kernels for the slowness model, based on first arrivals and reflection arrivals, respectively, which demonstrate the sensitivity of first and reflection arrivals to distinct subsurface structure within the study region. Figure 4g shows the inversion result based only on first arrivals. Velocity anomalies at shallow depths (above ~20 km) can be well

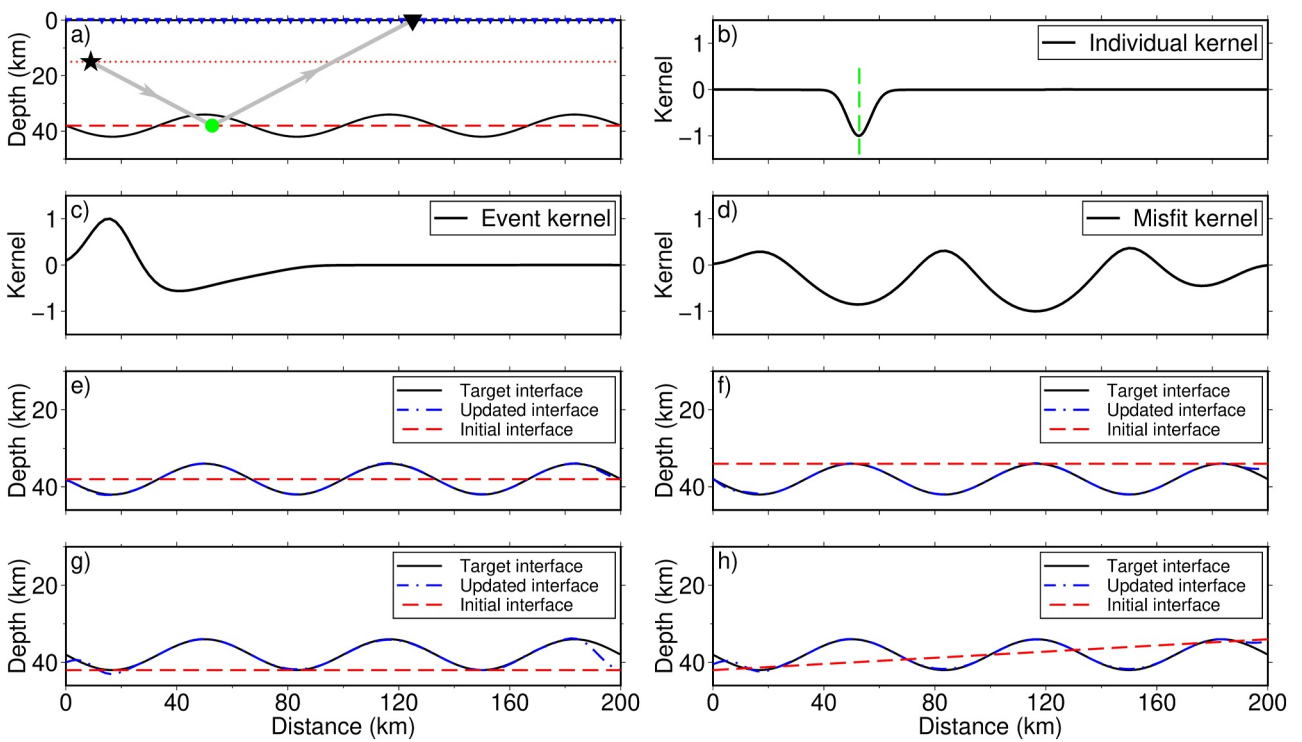


**Figure 5.** 3D synthetic test for interface inversion at the profile  $y = 5$  km. (a) The black solid line is the target interface, and the red dotted line is the initial interface. The black star and inverted triangle represent the considered source-receiver pair. The propagation path of the reflection wave is shown as the gray line, with a green dot indicating the location of the reflection point. (b) The calculated individual kernel based on the source-receiver pair in (a). The vertical green dotted line marks the location of the reflection point based on the initial interface. (c) The calculated event kernel based on the source in (a). (d) The calculated misfit kernel based on the initial model, which is obtained by summing all event kernels. (e)–(h) Updated interfaces (blue curves) based on different initial interfaces (red curves).

reconstructed. Nonetheless, due to the limited penetration of direct waves into deep structures, the velocity anomalies below 20 km are scarcely revealed. This highlights the effectiveness of incorporating reflection data in enhancing the resolution of tomographic results. Figure 4h displays the imaging results using only reflection arrivals. As reflection waves follow distinct propagation paths from direct waves, they can provide independent constraints for the deep region. Nevertheless, the imaging resolution is comparatively lower in the left and right margins of the study region, as well as in the shallow part, when compared to the first arrival-based imaging. The joint inversion (Figure 4i) using first and reflection arrivals can effectively reconstruct the velocity anomaly over the entire depth range.

### 3.2. Interface Inversion

Next, we give an example of interface inversion using only reflection arrivals. We consider the same sources and receivers distribution as in Section 3.1. The velocity model is assumed to be a known constant model ( $v_0 = 6$  km/s), and the target interface topography (Figure 5a) is generated by

$$d(x,y) = 4 \sin(0.03\pi x) + 38. \quad (50)$$

Similar to the previous test, we need to solve forward eikonal Equations 7b and 7c (to determine  $T_n^I(\xi)$ ,  $T_n^R(\xi)$ ) and adjoint Equations 14 and 15 (to determine  $P_n^R(\xi)$ ,  $P_n^I(\xi)$ ) for each source. Subsequently, the sensitivity kernel with respect to interface topography can be calculated based on Equation 46.

In Figures 5b–5d, the individual kernel, event kernel, and misfit kernel about the interface topography are presented. The individual kernel (Figure 5b) exhibits sensitivity predominantly in the vicinity of the theoretical reflection point. Note that the sensitivity kernel shows singularities at the source and receiver locations, which require masking or smoothing during the calculation. For each source-receiver pair, the advancement or delay of the reflection arrival determines whether the interface close to the theoretical reflection point ought to be adjusted

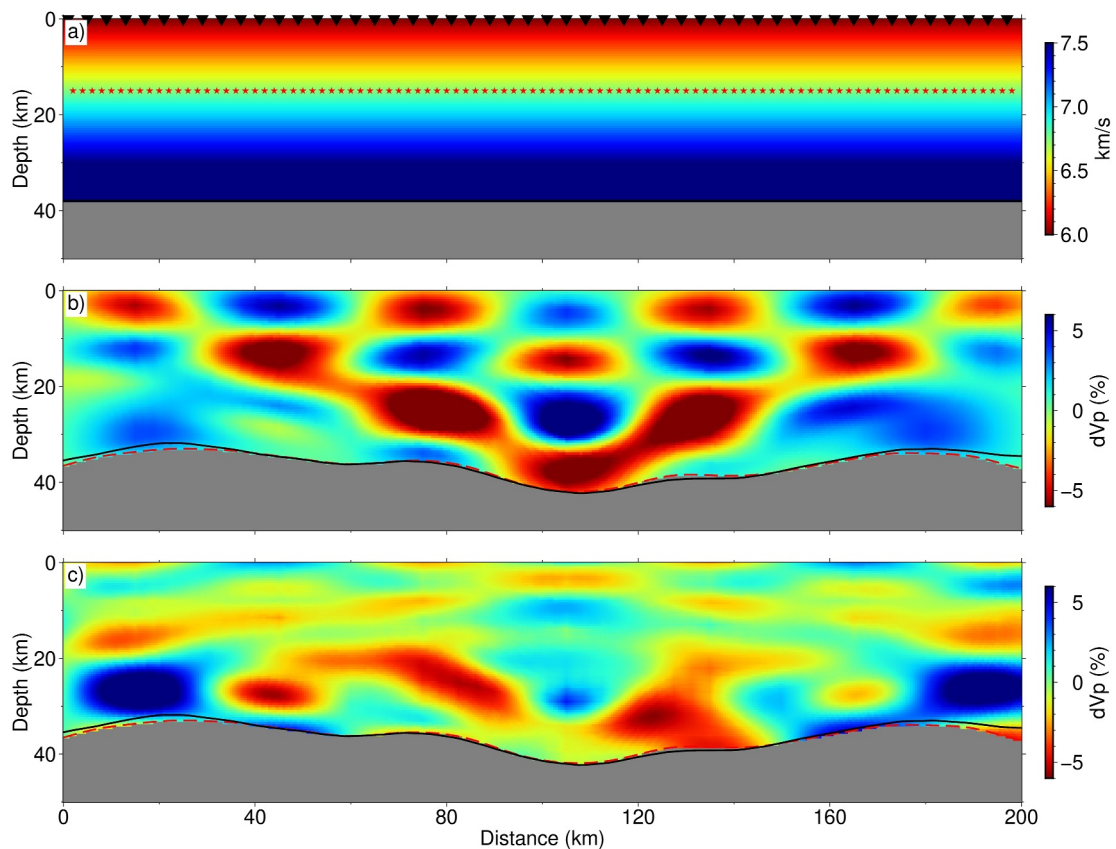


**Figure 6.** 3D synthetic test considering the joint inversion for velocity and interface topography, at the profile  $y = 5$  km. (a) Sources (red stars) and receivers (black inverted triangles) used in the inversion. The initial velocity model increases linearly with depth, and the initial interface is horizontal. (b) Imaged velocity anomalies and interface topography, where the black line marks the target interface and the red dotted line represents the interface obtained by inversion. (c) Difference between the recovered  $V_p$  perturbation and the target  $V_p$  perturbation.

downwards or upwards. The event kernel (Figure 5c), similar to slowness inversion, is obtained by linear superposition of individual kernels, and the same holds for the misfit kernel (Figure 5d). Figures 5e–5h exhibit a series of inversion outcomes using different initial interface topographies, illustrating the capability of the proposed method to constrain the interface topography with sufficient reflection data coverage.

### 3.3. Joint Inversion

Next, we consider the joint inversion for the slowness model and interface topography. A horizontal interface  $d_0 = 38$  km and a linear increasing velocity in Equation 48 are considered as the initial model. The target model is represented in Figure 3b, containing alternating high and low-velocity perturbations (Equation 49) imposed on the initial velocity model, along with an undulating interface.

We conduct joint inversion based on Algorithm 3. In this process, the sensitivity kernel for the slowness model incorporates the contribution of first arrivals and reflection arrivals, whereas the sensitivity kernel for the interface topography is completely determined by reflection arrivals. The final tomographic results are displayed in Figure 6b. It can be observed that the reconstructed interface topography (indicated by the red dotted line) aligns well with the target interface topography (represented by the black line). The shallow velocity structures (above approximately 20 km) are accurately determined. While the deep structures are partially recovered, the strong coupling between interface and near-interface velocities leads to smearing in the tomographic results (Figure 6c). In practical applications, other methods can be used to provide independent constraints for the velocity or interface. For example, the receiver function analysis is widely considered to determine the topography of the underground interface (e.g., Ammon, 1991; Langston, 1979; Owens et al., 1984; Schmandt et al., 2015; L. Zhu & Kanamori, 2000), which can provide good prior information and alleviate the impact of the strong coupling

between velocity and interface in the inversion (Li et al., 2024; Wu et al., 2022). Nevertheless, uncertainty estimation of joint inversion remains an important topic that needs to be carefully considered in future studies.

## 4. Application in Central California Near Parkfield

### 4.1. Background and Motivation

The main purpose of this section is to demonstrate the application of the proposed method in the joint inversion for velocity structure and interface topography in regional-scale traveltimes tomography. Similar to J. Chen et al. (2023) and Tong (2021b), we chose the region of central California near Parkfield as the test site. Since the Fort Tejon earthquake in 1857, this region has experienced seven earthquakes with magnitudes exceeding 6.0 at an average interval of 24.5 years, with the most recent one occurring in 2004 (Bakun et al., 2005). Many previous studies have identified the pronounced velocity contrast along the San Andreas Fault (SAF) (e.g., Eberhart-Phillips & Michael, 1993; Thurber et al., 2006). The southwestern side predominantly exhibits high-velocity structures, corresponding to the Salinian terrane, which is mainly composed of granite. In contrast, the northeastern side shows lower velocities, primarily consisting of the Franciscan Complex and the Great Valley Sequence (Audet, 2015; Page et al., 1998; Zeng et al., 2016). Based on variations in surface creeping rates, the SAF within the study area can be broadly divided into three segments: the northwestern creeping segment, the southeastern locked segment, and the transitional Parkfield segment in between (Lippoldt et al., 2017; Shelly & Hardebeck, 2010; Titus et al., 2006). More specifically, the creep rates decrease from about 30 mm per year northwest of SAFOD to less than 5 mm per year southeast of Cholame (Titus et al., 2006) (Figure 7a). Active geophysical surveys conducted in the SAFOD region provided high-resolution imaging of the shallow crustal structure across the SAF, revealing complex erosion and fault topography (e.g., Bleibinhaus et al., 2007; Hole et al., 2006). Due to the unique geological structure of the Parkfield region, various seismic phenomena have been observed, including regular earthquakes, repeating microearthquakes, non-volcanic tremors, and low-frequency earthquakes (LFEs) (Shelly, 2017; Turner et al., 2015). LFEs are observed at depths ranging from ~16–30 km in the lower crust, and some events even occurred in the uppermost mantle (Shelly, 2017). In this study, we attempt to constrain the lower crustal structure of the study area using the Moho-reflected PmP arrivals based on the proposed method, thereby offering new insight into the occurrence of LFEs along the SAF in the Parkfield region.

### 4.2. Data and Initial Model

The study region is the oblique area outlined by yellow lines in Figure 7, centered at (35.6°N, 120.45°W) and rotated counterclockwise by 30°, thus forming an approximately 4.2° by 1.4° rectangular region. There are two types of data used for joint inversion: the first P-wave traveltimes data and the PmP-wave traveltimes data. The initial data set of first-P arrivals comes from J. Chen et al. (2023), which are downloaded from the Northern California Earthquake Data Center (NCEDC, 2014) and the Southern California Earthquake Data Center (SCEDC, 2013). This data set achieved uniform and dense data coverage within the study area. By limiting the critical epicentral distances for Pn arrivals at different source depths, we excluded potential Pn arrivals from the initial data set (Text S2, Figures S1 and S2 in Supporting Information S1). Ultimately, approximately 1.1 million first-P arrivals originating from 33,051 earthquakes and recorded by 555 stations (Figure 7c), are used to constrain the upper crustal P-wave velocity structure. For reflection arrivals, we first downloaded three-component waveforms of earthquakes with magnitudes 2.0–5.0 and depths not exceeding 20 km within the study region between January 2000 and February 2024 from the Incorporated Research Institutions for Seismology Data Management Center (IRIS DMC), and then identified the most likely PmP signals by strict selection criteria (Text S3 in Supporting Information S1). One can also refer to Li et al. (2022) for a more detailed introduction. Figure 8 displays some manually picked PmP arrivals at station CIPHL. Text S4 in Supporting Information S1 provides more analysis and synthetic tests for the verification of PmP signals (Figures S3–S8 in Supporting Information S1). In total, we manually picked 7,070 PmP arrivals, which were derived from 4,070 earthquakes and recorded by 127 stations (Figure 7d). This data set is mainly used to constrain the lower-crust velocity structure and Moho discontinuity.

A well-established initial model is crucial for the correct convergence of inversion. In this study, we construct a one-dimensional velocity model coupling the Moho discontinuity within the study region, building upon previous research. More specifically, we utilize the Moho discontinuity model constrained by the joint inversion of receiver functions and surface wave dispersions (Schmandt et al., 2015) as the initial Moho discontinuity model

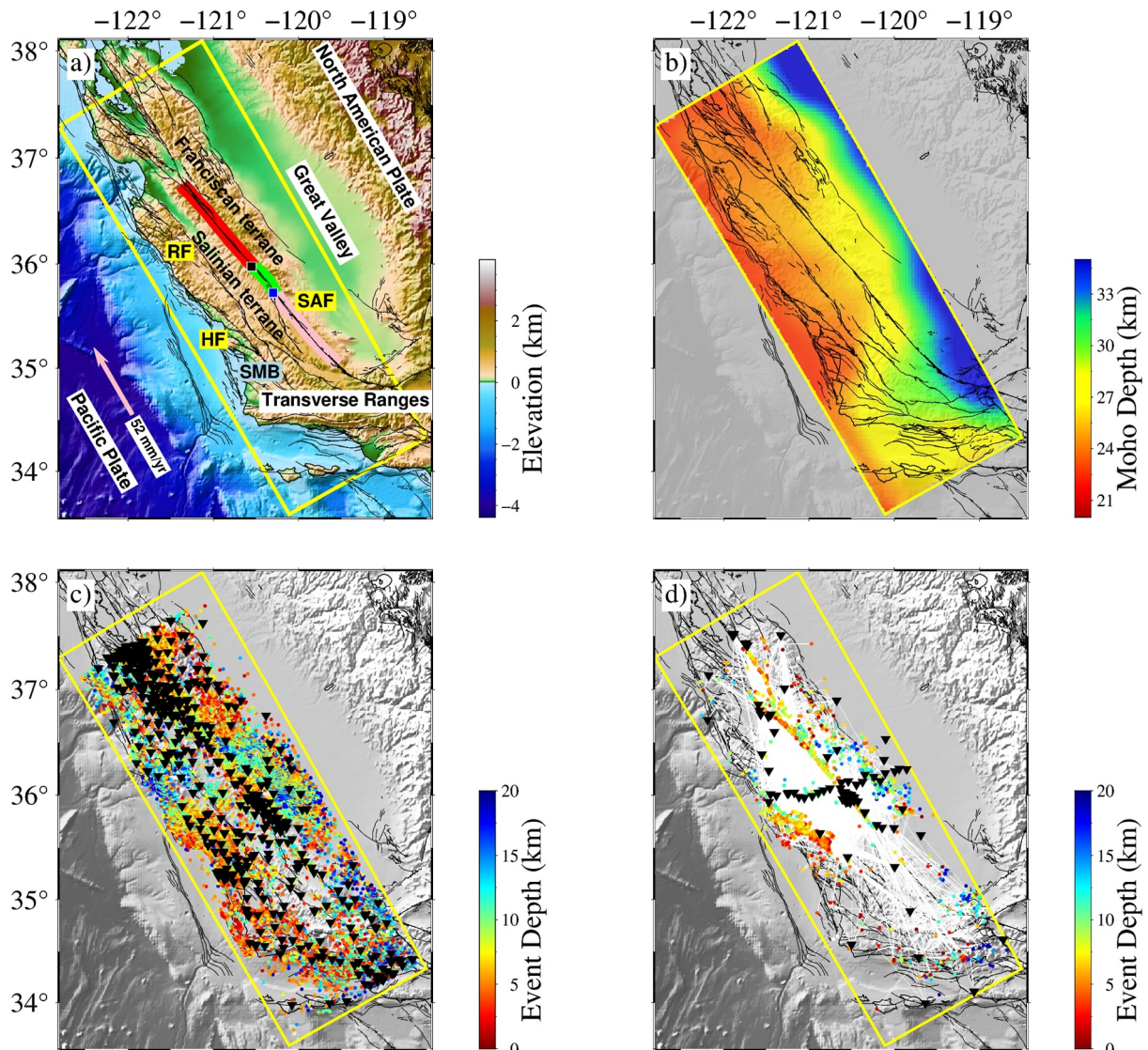


**Figure 7.** (a) Tectonic setting in central California near Parkfield. The yellow line outlines the simulated region. Black lines mark active faults within the study area, some of which are HF (the offshore Hosgri Fault), RF (the Rinconada Fault), and SAF (San Andreas Fault). The red, green, and pink segments mark the creeping, transitional, and locked segments of the SAF, respectively. The black and blue squares indicate the positions of the SAFOD and Cholame, respectively. SMB: Santa Maria Basin. (b) The initial Moho discontinuity model, which is constructed based on Schmandt et al. (2015). (c) Data distribution of first-P arrivals. The black inverted triangles denote the stations, while the colored dots represent earthquakes at various depths. (d) Similar to (c) but considering the data distribution of PmP arrivals. The source-station pairs that provide PmP arrivals are connected by white lines.

( $d_0$ ). The average crustal thickness in the simulated region is approximately 27.3 km, with a general increase in thickness from the offshore regions to the inland areas (Figure 7b). The initial velocity model ( $v_0$ ) mainly refers to J. Chen et al. (2023) and Tong (2021b). We considered a three-layered velocity structure, including the sedimentary layer above 4 km, the upper crust down to 16 km, and the lower crust from 16 km to the Moho discontinuity, which has constant velocity values of 4.17, 6.05, and 6.59 km/s, respectively. A Gaussian smoother with a mean of 0 km and a standard deviation of 0.4 km is applied to smooth transitions between layers. Consequently, the body-fitted grid is generated in the physical domain based on such an initial model (Figure S9 in Supporting Information S1), which is used to calculate the forward traveltime field and adjoint field in subsequent iterations. The grid spacing in the computational domain is  $2 \text{ km} \times 2 \text{ km} \times 1 \text{ km}$ . Here we employ an upwind fast-sweeping scheme to solve the factored eikonal equation. On an i9-13900K processor, it takes approximately 40 min to complete one iteration using first arrivals (including 555 forward and adjoint simulations). For reflection arrivals, one iteration takes about 17 min, with 127 forward and adjoint simulations.

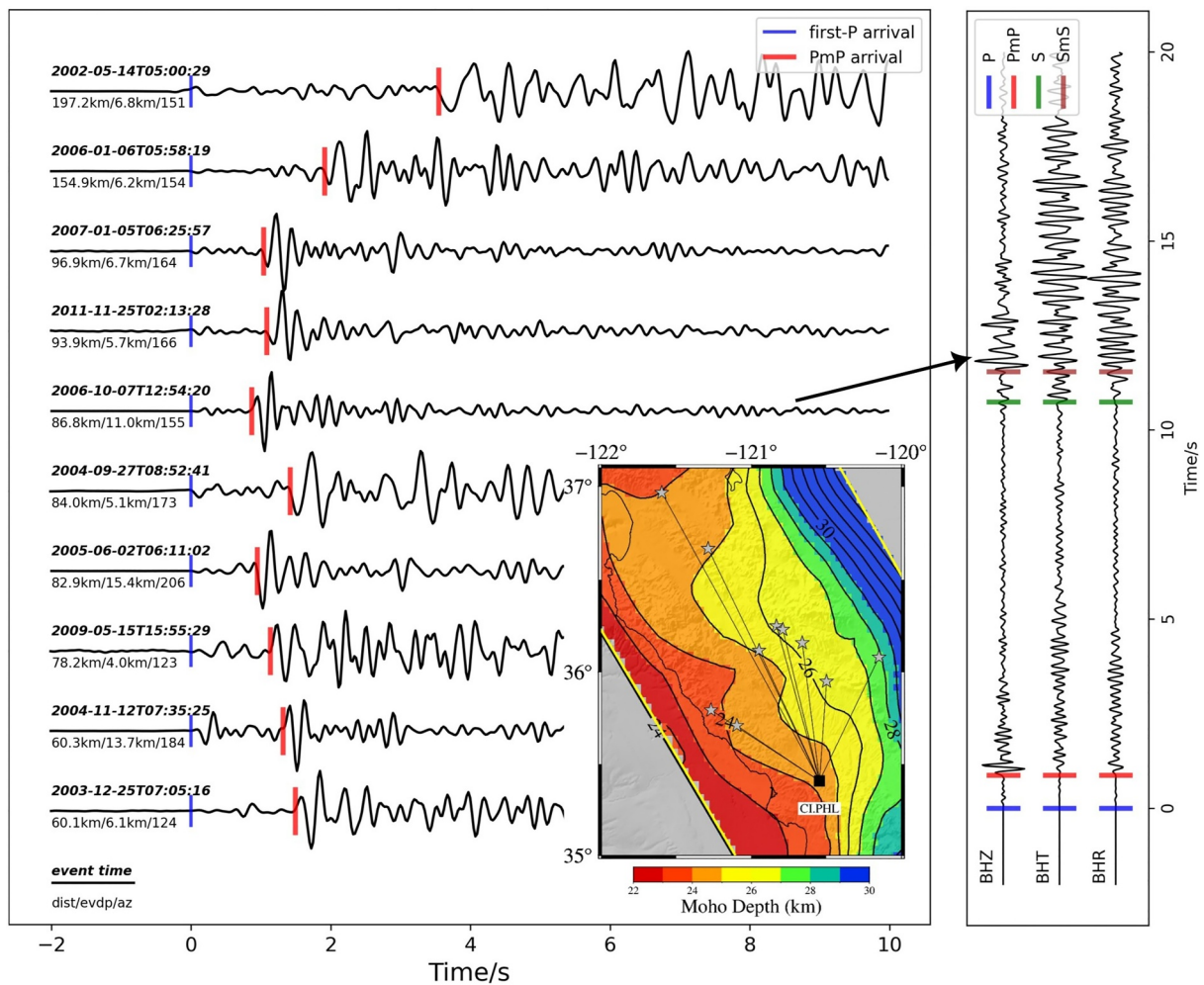


**Figure 8.** Some manually picked PmP arrivals at station CI.PHL (black square in the lower right sub-figure). Each seismic record (Z-component) is aligned at the first-P arrival time (shown by the blue line), and the red line represents the PmP arrival time. The right sub-figure shows three-component (Z, R, T) waveforms of a specific earthquake recorded at this station.

#### 4.3. Inversion Procedures and Checkerboard Test

We first perform a checkerboard test to estimate the resolution of the data utilized in our study. The target model is constructed by assigning alternating positive and negative perturbations to the velocity model and Moho discontinuity simultaneously, as defined by

$$v_T(x,y,z) = v_0(x,y,z)(1 + \delta v(x,y,z)) \\ = \begin{cases} v_0(x,y,z)\left(1 + 0.08 \sin\left(2\pi \frac{x}{1.4^\circ}\right) \sin\left(6\pi \frac{y}{4.2^\circ}\right) \sin\left(2\pi \frac{z}{16}\right)\right), & z \leq 16, \\ v_0(x,y,z)\left(1 + 0.08 \sin\left(2\pi \frac{x}{1.4^\circ}\right) \sin\left(6\pi \frac{y}{4.2^\circ}\right) \sin\left(\pi \frac{z - 16}{16}\right)\right), & z > 16. \end{cases}, \quad (51)$$

$$d_T(x,y) = d_0(x,y) + \delta d(x,y) = d_0(x,y) + 2 \sin\left(2\pi \frac{x}{1.4^\circ}\right) \sin\left(4\pi \frac{y}{4.2^\circ}\right), \quad (52)$$

which indicates that the maximum amplitude of the velocity perturbation ( $\delta v$ ) is 8%, and the perturbation of the Moho discontinuity ( $\delta d$ ) does not exceed  $\pm 2$  km. The first-P arrivals and PmP arrivals are generated based on  $v_T$  and  $d_T$ , and they maintain the same data coverage as the observed data used in the inversion. The inversion

strategy is designed as follows: In the first 40 iterations, we only use first-P arrivals to determine a stable velocity model  $v_{c1}$  that can constrain the upper crustal structure. The Moho discontinuity will not be updated at this stage. After that, we loop through the following sub-iteration groups: each group of sub-iterations includes five iterations using PmP arrivals to update the velocity model (Algorithm 1), five iterations using first-P arrivals to update the velocity model, and five iterations using PmP arrivals to update the Moho discontinuity (Algorithm 2). The utilization of this kind of alternating inversion strategy allows for the avoidance of subjectively determining weighting coefficients due to the data set imbalance between first-P and PmP arrivals. To ensure that both data sets are effectively inverted, we obtain the final velocity model  $v_{c2}$  and the Moho discontinuity model  $d_{c2}$  after 125 iterations. It means that we performed six complete sub-iteration groups and stopped the iteration after using first-P arrivals to update the velocity model in the last sub-iteration group.

Compared with the initial model, the standard deviation of the first-P (PmP) traveltime residuals decreases from 0.176 (0.175) to 0.025 (0.027) s, demonstrating that the updated model simultaneously provides a better fit to both types of traveltime data. Figure S10 in Supporting Information S1 displays the horizontal sections of the velocity perturbations of the target model ( $v_T$ ), the velocity model considering only first-P arrivals ( $v_{c1}$ ), and the final velocity model ( $v_{c2}$ ) compared to the initial model  $v_0$  at different depths. Figure 9 shows some vertical sections of  $v_{c1}$  and  $v_{c2}$ , respectively. Due to the good constraints provided by first-P arrivals, most upper crustal velocity anomalies (<16 km) can be recovered well, except for the southwest corner of the study region (Figure 9, P3), where the number of earthquakes and stations is limited (Figure 7c). PmP arrivals provide independent constraints on the subsurface structures that are distinct from those obtained from first-P arrivals. In areas where PmP waves traverse through, the lower crustal velocity structure and Moho discontinuity can also be further constrained. Specifically, by comparing the velocity profiles of the inversion results of considering first-P and PmP arrivals with those considering only first-P arrivals (Figure 9 P2–P3, Q1–Q2), the contribution of PmP arrivals in constraining the lower crustal velocity structures can be evidently observed. For the same first-P arrivals data set, J. Chen et al. (2023) also mentioned that the well-recovered depth is limited to above 14 km. PmP arrivals can constrain lower crustal velocity anomalies without compromising the imaging resolution of the upper crust (Figure 9). On the other hand, although there may exist trade-off between the lower crustal velocity and the Moho discontinuity, the input Moho depth anomalies can be well recovered based on the current PmP arrivals (Figures 9b and 9c). Furthermore, we conducted an additional synthetic test to evaluate the impact of picking error on the inversion results (Figures S11 and S12 in Supporting Information S1). The findings demonstrate that the inversion results are stable in the presence of reasonable levels of data noise. Overall, by inverting both the first-P and PmP arrivals jointly, the subsurface velocity and interface anomalies within the study area can be well recovered, indicating that the selected data can effectively constrain the crustal velocity structure and the Moho discontinuity in central California near Parkfield.

Considering the possible coupling between the source location and the velocity structure, we conducted another synthetic test to evaluate the impact of source uncertainty on the inversion results. First, we downloaded the earthquake catalog relocated using the double-difference (DD) method in the study region from NCEDC (Waldhauser & Schaff, 2008), which has a relatively high location accuracy. There are about 20,000 earthquakes in both the DD catalog and the catalog we use. Based on this common earthquake catalog, we calculated the inconsistency between the two catalogs in terms of longitude, latitude, depth, and origin time, respectively. The mean and standard deviation are  $-0.02 \text{ km}/0.90 \text{ km}$  for longitude,  $0.02 \text{ km}/0.63 \text{ km}$  for latitude,  $-0.15 \text{ km}/1.04 \text{ km}$  for depth, and  $-0.0085 \text{ s}/0.14 \text{ s}$  for origin time. We generated random deviation following the Gaussian distribution based on the above parameters and added them to the source parameters to create perturbed source locations (Figure S13 in Supporting Information S1). The observed data for the checkerboard test is generated from the correct source locations, while the perturbed source locations are used for the inversion. This approach allows us to evaluate whether the input velocity and interface anomalies can be effectively recovered if the sources are deviated. Figures S14 and S15 in Supporting Information S1 illustrate a comparison of imaging results based on the correct and perturbed sources, respectively. The results exhibit a high degree of similarity, indicating that the source uncertainty has a limited impact on this work.

#### 4.4. Results, Discussions, and Future Works

We implement exactly the same inversion strategy used for the checkerboard test to invert the selected first-P and PmP arrivals. In each iteration, only the data satisfying the condition  $|t_{obs} - t_{syn}| \leq 3 \text{ s}$  are utilized. During the initial 40 iterations, only the first-P arrivals were considered, leading to a decrease in the misfit function from

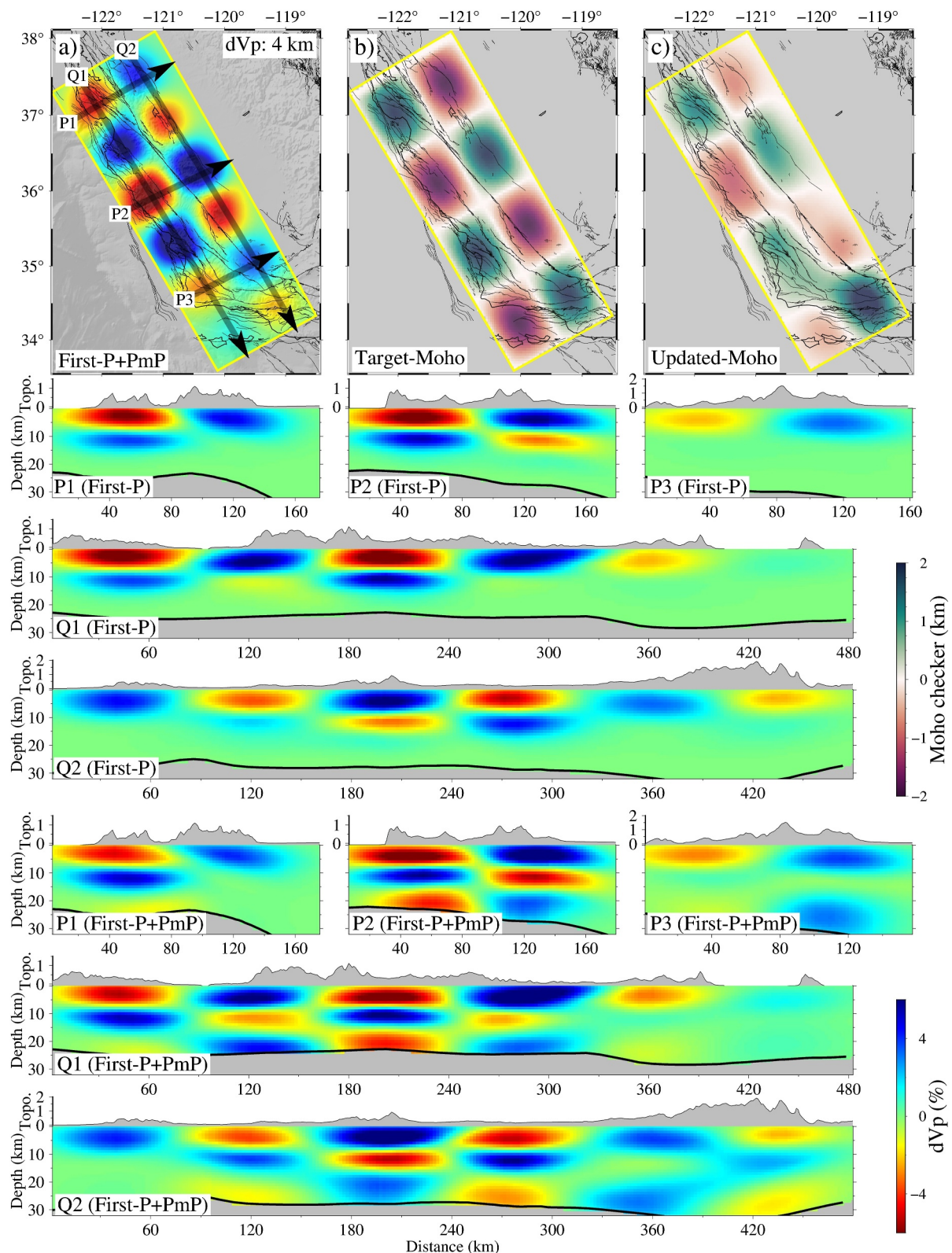
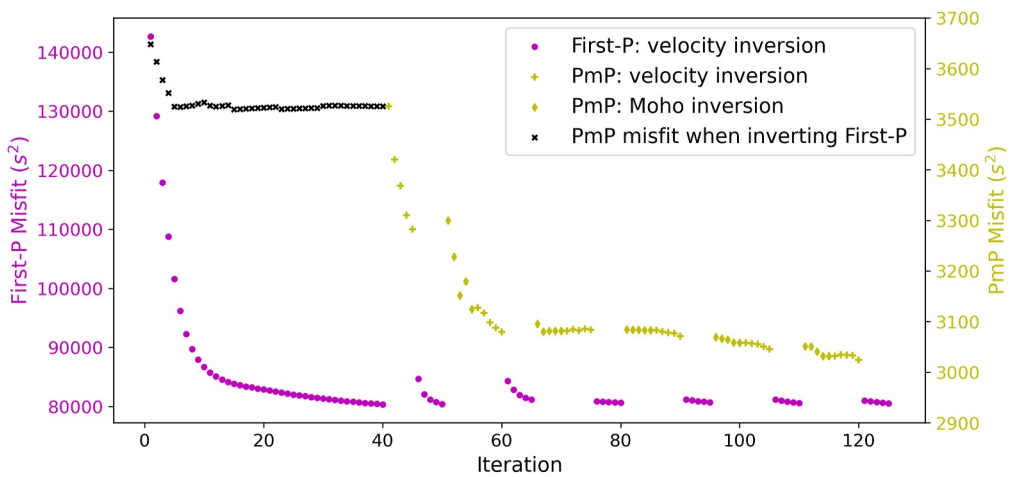


Figure 9.

142,665 s<sup>2</sup> to 80,352 s<sup>2</sup>. This stage yields a stable upper crustal velocity structure within the study area (denoted as  $v_{m1}$ ). Notably, after each iteration of updating the velocity model, we calculate synthetic PmP arrivals based on the revised velocity model and compare them with the observed PmP arrivals to compute the traveltime residuals. The updated velocity model, derived using first-P arrivals, also achieved a better fit to the observed PmP arrivals (Figure 10), demonstrating the compatibility of the first-P and PmP arrivals used in the inversion. Subsequently, PmP arrivals and first-P arrivals are alternately inverted to update the velocity model and Moho discontinuity. After 125 iterations, we obtained the final tomographic velocity-Moho model (denoted as  $v_{m2}$  and  $d_{m2}$ , respectively). Based on the robust shallow velocity structure obtained in the previous stage, the first-P misfit function remained generally stable compared to  $v_{m1}$  (from 80,352 s<sup>2</sup> to 80,510 s<sup>2</sup>), while the PmP misfit function decreased by approximately 17% compared to the initial model (from 3,648 s<sup>2</sup> to 3,024 s<sup>2</sup>) (Figure 10). After the iteration is completed, the standard deviation of the first-P (PmP) traveltime residuals decreases from 0.50 (1.01) to 0.38 (0.93) s (Figure S16 in Supporting Information S1), and the RMS value of the traveltime residuals decreases from 0.51 (1.02) to 0.38 (0.93) s for first-P (PmP) arrivals.

The updated Moho discontinuity model  $d_{m2}$  is shown in Figure 11. Considering that the receiver function method could already provide a good prior Moho discontinuity model for the inversion, we limited the magnitude of interface updates to within  $\pm 2$  km. Consequently, the inversion primarily fine-tunes the Moho depth, suggesting crustal thickening beneath the Franciscan terrane and a slightly thinner crust in the southern part of the study area, compared to the initial Moho depth. Below we mainly discuss the velocity anomalies of tomographic results. Figure 12 shows the horizontal sections of the P-wave velocity perturbations of  $v_{m1}$  and  $v_{m2}$  relative to the initial model at different depths. Meanwhile, Figure 13 displays vertical cross-sections of the final model.  $v_{m1}$  and  $v_{m2}$  exhibit a high degree of similarity in the shallow part (e.g., <10 km), with the most notable feature being the strong velocity contrast across the creeping to transitional Parkfield segment along the SAF (Figures 12a–12f), which is consistent with previous studies (Thurber et al., 2006; Tong, 2021b). This contrast aligns well with the surface trace of the SAF, effectively separating the Franciscan terrane (low-velocity body) to the northeast from the Salinian terrane (high-velocity body) to the southwest. A high-velocity body has been imaged beneath the Transverse Range at the southeastern edge of the study region, which can also be found in previous research (J. Chen et al., 2023; Lin et al., 2010). In the central-western part of the study area at about 35–35.5°N, a relatively weak low-velocity anomaly is detected beneath the Santa Maria Basin, extending slightly northward down to a depth of 10 km, which has been reported before (Tong, 2021b) and could be associated with the sediments and northwest-southeast trending faults. The imaging resolution of the first-P arrivals used in this study is limited to about 14 km (Figure 11; J. Chen et al., 2023). Therefore, the tomographic results for the middle to lower crust are primarily contributed by PmP arrivals (Figure 9 and Figure S10 in Supporting Information S1). The middle to lower crust in the southeastern part exhibits high-velocity anomalies that gradually weaken with depth, connecting with that beneath the Transverse Ranges (Figures 12h, 12j, and 12l). At approximately 37°N, a significant low-velocity anomaly is identified beneath and to the east of the SAF, extending continuously to the Moho discontinuity (Figures 12h, 12j, and 12l). This prominent low-velocity anomaly is also observed in a regional surface wave tomographic model (Jiang et al., 2018). Besides, another two low-velocity anomalies are also detected in the lower crust (Figures 12j and 12l). One is crossing the SAF beneath the southern part of the creeping section between 35.5–36.5°N. It approaches the coastline to the southwest and extends to 40 km northeast of the SAF. Such pattern is also well visible in a local surface wave tomography model (Lippoldt et al., 2017), and present in a local body-wave travelttime tomography which involves various kinds of data sets including regular earthquakes, shots, quarry blasts, and LFEs (Zeng et al., 2016). The other imaged deep low-velocity body dominates at around 35.3°N to the southwest of the SAF, and its margin also crosses the SAF. This feature can also be observed in the tomographic results from Lippoldt et al. (2017) and Zeng et al. (2016). In addition, a double-difference tomography work (Zhang et al., 2017) also images low-velocity anomalies beneath and to the southwest of the SAF in this area, though the resolved low-velocity body has a smaller spatial scale compared to our result.

**Figure 9.** (a) Horizontal section of velocity perturbation obtained by joint inversion at a depth of 4 km. The black arrows (P1–P3, Q1–Q2) depict the locations of the vertical profiles drawn in the sub-figures below. Sub-figures labeled “First-P” indicate the tomographic results based only on first-P arrivals (i.e., model  $v_{c1}$ ), while the thick black line marks the depth of the initial Moho discontinuity ( $d_0$ ) along the corresponding survey line. Similarly, sub-figures labeled “First-P + PmP” show vertical profiles of the final inversion result (i.e., the model  $v_{c2}$ ), and the thick black lines mark the depth of the Moho discontinuity updated by the inversion (i.e., the model  $d_{c2}$ ). (b) The anomaly of the target Moho discontinuity relative to the initial Moho discontinuity ( $\delta d$ ). (c) The anomaly of the Moho discontinuity after inversion relative to the initial Moho discontinuity.



**Figure 10.** The misfit function curve during the inversion. Magenta dots represent the misfit function associated with first-P arrivals during the iteration. Black crosses symbolize the misfit of the PmP data after each update of the velocity model using the first-P arrival. Yellow crosses mark the misfit when using PmP arrivals to update the velocity structure, while yellow diamonds indicate the misfit when using PmP arrivals data to update Moho discontinuity.

Previous studies have located the LFE families in the Parkfield region, covering the creeping to the locked segments of the SAF, with depths primarily concentrated in the lower crust at 18–28 km (Shelly & Hardebeck, 2010). There are already multiple pieces of evidence suggesting the presence of fluids in the lower crust near the SAF, either from geophysical images like the low-velocity structure (Lippoldt et al., 2017), high Vp/Vs ratio (Ozacar & Zandt, 2009), and low electrical resistivity zone (Becken et al., 2011), or from the mineral analysis sampled from outcrops, that is, the existence of weak talc which is thought to be generated from hydrothermal fluids interacting with serpentinite (Moore & Rymer, 2007). The S-wave velocity structure of the

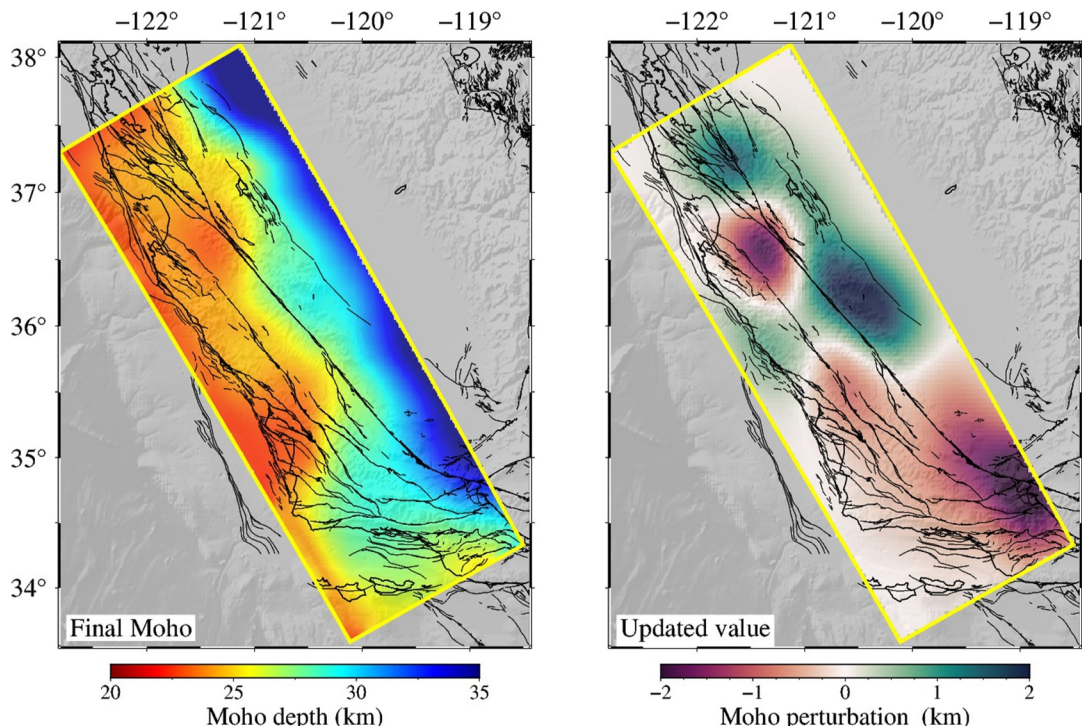


**Figure 11.** Left: the Moho depth in the study area obtained by inversion. Right: the difference between the final Moho and the initial Moho, which is obtained by subtracting the initial Moho depth from the updated Moho depth.

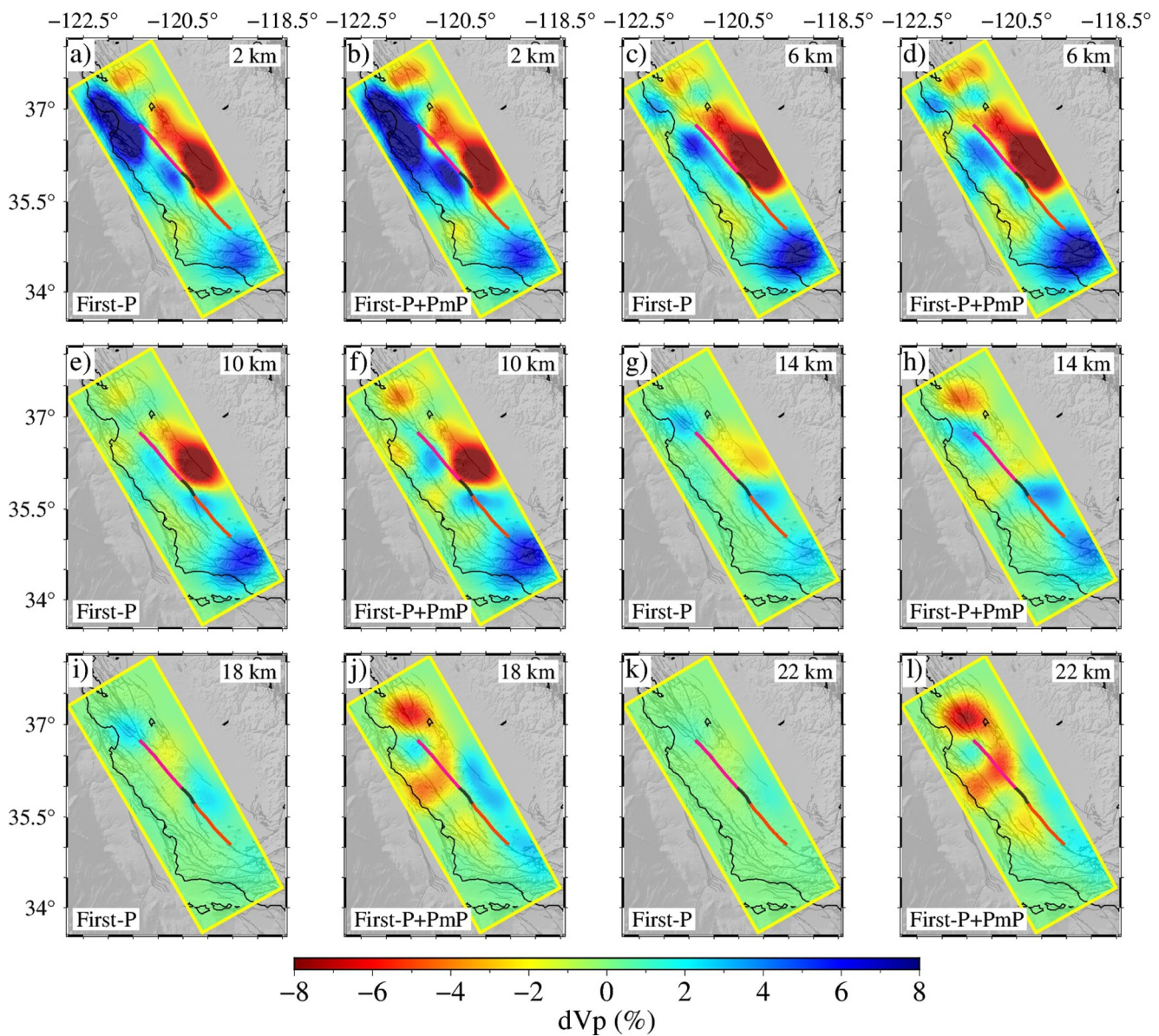


**Figure 12.** Horizontal sections of the P-wave velocity perturbation to the initial model. The colored lines mark the creeping, transitional, and locked segments of the SAF (from northwest to southeast). (a, c, e, g, i, and k) Inversion results (model  $v_{m1}$ ) after 40 iterations (considering only first-P arrivals) at different depths. (b, d, f, h, j, and l) Final inversion results (model  $v_{m2}$ ) after 125 iterations (considering first-P and PmP arrivals) at different depths.

lower crust in this region has been constrained by different data or methods, such as LFEs differential arrival time (Zeng et al., 2016), differential arrival time of non-volcanic tremors (Zhang et al., 2017), and surface wave ambient noise tomography (Lippoldt et al., 2017). These results show that LFEs are primarily located within imaged low-velocity bodies, suggesting that the occurrence of LFEs may be closely related to high-pressure pore fluids from dehydration reactions (Nadeau & Guilhem, 2009; Thomas et al., 2009). Becken et al. (2011) identified large-scale low-resistivity structures in the lower crust and uppermost mantle, they interpreted the low-resistivity zone as being under high fluid pressure, facilitating brittle failure at lower crustal depth. In this study, we used PmP arrivals to constrain the P-wave velocity structure of the lower crust. The imaged low-velocity bodies generally coincide with the variation of LFEs along the fault strike (Figure 13 P3–P6, Q1–Q3). Since completely independent data are utilized, our tomographic imaging results provide new evidence for the possible presence of fluid or talc-bearing serpentinites, further suggesting their significant roles in the generation of LFEs in the Parkfield region. There are some additional interesting observations about the two imaged low-velocity bodies.

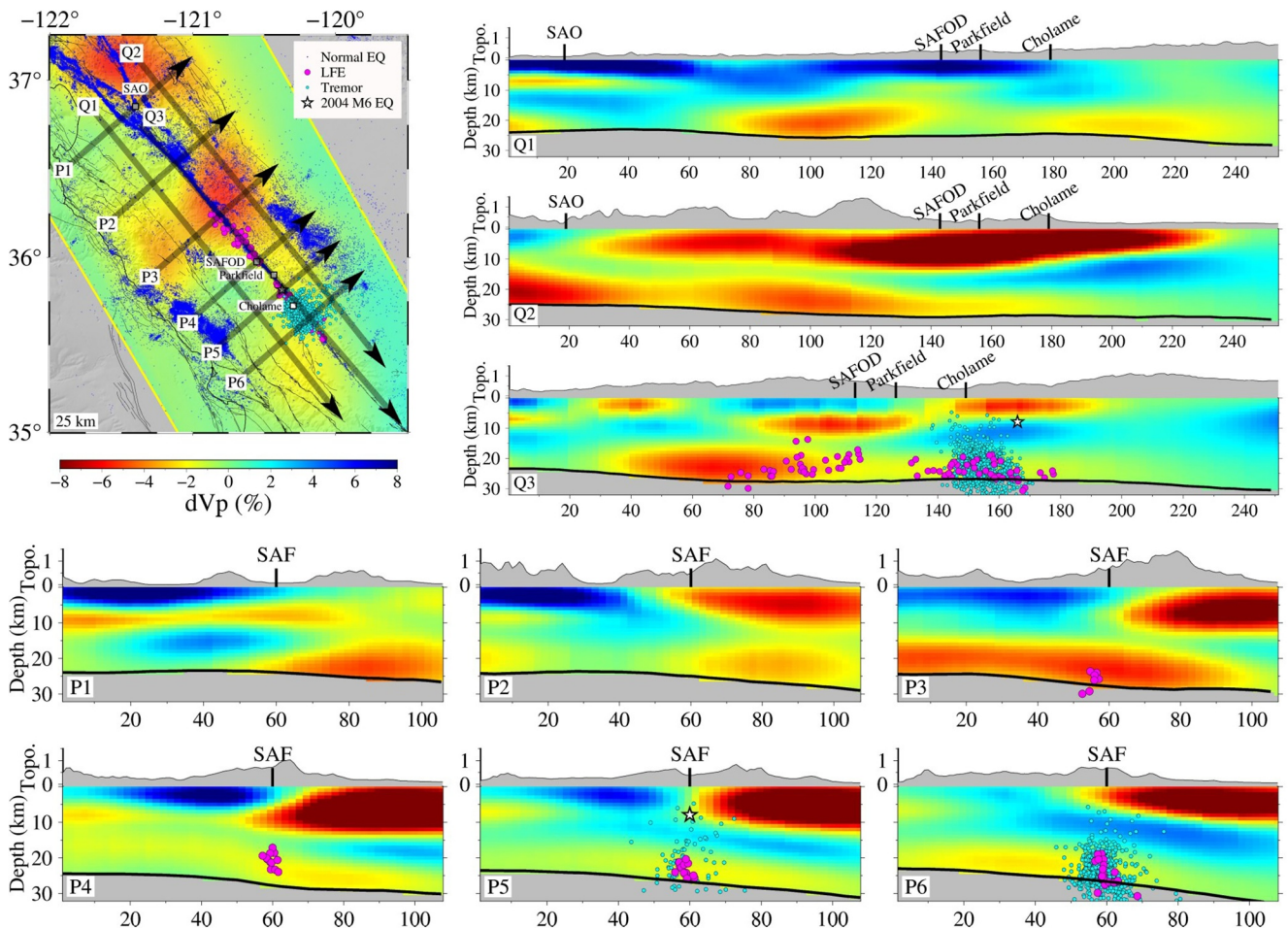


**Figure 13.** Some vertical sections of the final inversion result ( $v_{m2}$ ), whose locations are given in the upper left sub-figure. The blue dots mark the locations of regular earthquakes in the study area provided by NCEDEC, and the magenta dots are low-frequency earthquakes located in Zeng et al. (2016). The green dots are tectonic tremor locations near Cholame (H. Guo et al., 2017). The white star marks the 2004  $M_w$  6.0 Parkfield earthquake.

The distribution of LFEs exhibits a notable gap beneath the transitional segment of the SAF (Figure 13; Shelly, 2017), which appears to align with the distinct low-velocity anomalies detected in our images (Figure 13 Q1, Q3). Moreover, previous studies suggested that the tremor amplitudes along the SAF exhibit rapid variations. Specifically, the tremor amplitude beneath Cholame is significantly higher overall than that in the northwest of Parkfield (Shelly & Hardebeck, 2010). This observation corresponds with the amplitude of the imaged low-velocity anomalies. The amplitude of the low-velocity anomaly beneath Cholame appears to be smaller than that on the other side (Figure 13 Q1, Q3), which may indicate mechanically stronger rocks there. Our tomographic images support that the tremor amplitude variations along the deep root of the SAF seem to reflect strength variations (Becken et al., 2011). These findings highlight the necessity for more comprehensive studies in the future to illuminate the intricate relationship between low-velocity anomalies and the occurrence of LFEs more accurately.

The reflection traveltime tomography conducted in the Parkfield region demonstrates the application scenarios of the proposed new method in crustal-scale tomographic imaging. While this study focuses solely on passive-source data, the method can be seamlessly extended to active-source surveys. Incorporating active-source data could significantly improve the tomographic resolution, given the source accuracy and dense data coverage. Future studies will attempt to incorporate such data to reveal fine-scale structures across the SAF. Additionally, the potential impact of other factors, such as earthquake locations and velocity anisotropy, will be considered in the inversion to further refine the tomographic models.

## 5. Conclusions

First arrivals of crustal earthquakes have been widely used to image shallow structures, but are insensitive to deeper velocity structures and interface topography because of their depth-limited propagation paths. Since reflection waves have different propagation paths, they can provide good constraints on deep structures to enhance imaging resolution. In this study, we propose a novel eikonal equation-based adjoint-state reflection travelttime tomography method for velocity and interface inversion. Compared with ray tracing-based methods, the predicted traveltimes calculated by solving an eikonal equation are more stable, so it is more likely to obtain high-precision tomographic results.

By considering a two-stage eikonal equation, we can efficiently calculate travelttime fields for predicting reflection arrivals. In order to deal with irregular interfaces, we map the physical domain with an undulating interface to a regular computational domain through coordinate transformation, so that the eikonal equation can be solved with high accuracy through uniform meshing in the computational domain. During this process, the original eikonal equation is converted into an anisotropic eikonal equation in the computational domain, with the interface topography in the physical domain encoded into anisotropic parameters in the computational domain.

For the inversion, we first derive the sensitivity kernel of the misfit function with respect to slowness through the adjoint-state method. This involves solving a two-stage forward equation and a two-stage adjoint equation to determine the gradient for each source. Consequently, the computational cost is only proportional to the number of sources and independent of the number of receivers. Furthermore, we formulate an explicit sensitivity kernel with respect to the interface topography, which benefits from the coordinate transformation that can equivalently convert the interface into anisotropic parameters. Specifically, since the interface topography is represented by anisotropic parameters in the computational domain, we establish a relationship between the perturbation of interface topography and the perturbation of anisotropic parameters. This connection is further linked with the perturbation of the misfit function, enabling the derivation of a specific form for the sensitivity kernel about the interface topography. Under such a framework, both slowness inversion and interface topography inversion avoid ray tracing. Based on the calculated sensitivity kernel about slowness or interface, we can use gradient-based methods to iteratively optimize the misfit function. The proposed method is validated through several synthetic tests of velocity and interface inversion. Based on the proposed method, we construct a new crustal velocity structure and Moho discontinuity model for the Parkfield region of central California by inverting traveltimes of both first-P and Moho-reflected PmP signals. The velocity structure of the upper crust is largely consistent with previous studies, revealing a strong velocity contrast across the SAF, which clearly presents the Franciscan complex to the northeast and the Salinian block to the southwest. The low-velocity anomalies imaged in the lower crust have good spatial correspondence with the along-strike variations of LFEs in the region, indicating that high fluid pressure may exist.

## Data Availability Statement

The seismic waveform data for picking PmP arrivals are downloaded through the IRIS Web Services (Trabant et al., 2012). The seismic networks used include: the 4E (Vernon & Orcutt, 2010); the BK (Northern California Earthquake Data Center, 2014); the CI (California Institute of Technology and United States Geological Survey Pasadena, 1926); the G (Institut de physique du globe de Paris (IPGP) & Ecole et Observatoire des Sciences de la Terre de Strasbourg (EOST), 1982); the GS (Albuquerque Seismological Laboratory (ASL)/USGS, 1980); the PB (Plate Boundary Observatory Borehole Seismic Network, available at <https://www.fdsn.org/networks/detail/PB/>); the TA (IRIS Transportable Array, 2003); the TO (MASE, 2007); the US (Albuquerque Seismological Laboratory (ASL)/USGS, 1990); the XN (Thurber & Roecker, 2000); the YH (Thurber & Roecker, 2004). The Northern California Earthquake Data Center (NCEDC, 2014) and the Southern California Earthquake Data Center (SCEDC, 2013) provide high-quality arrival time data used in this study. Figures are made by the Generic Mapping Tool (Wessel et al., 2019) and Matplotlib (Hunter, 2007). The final tomographic model, along with the PmP arrivals utilized in the inversion, are available on Zenodo (G. Chen et al., 2024).

## Acknowledgments

We thank Fenglin Niu (Editor), Nori Nakata (Associate Editor), and two anonymous reviewers for their constructive and valuable comments, which have greatly improved the paper. This work is funded by Minister of Education, Singapore, under its MOE AcRF Tier-2 Grant (MOE-T2EP2012-0008) and its MOE AcRF Tier-1 Thematic Grant (RT12/22). GXC is also supported by China Scholarship Council and CEE Departmental Postdoctoral Fellowship Scheme of the Hong Kong Polytechnic University. The codes that support the findings of this study are available from the corresponding author, PT, upon reasonable request.

## References

- Aki, K., & Lee, W. H. K. (1976). Determination of three-dimensional velocity anomalies under a seismic array using first P arrival times from local earthquakes: I. A homogeneous initial model. *Journal of Geophysical Research*, 81(23), 4381–4399. <https://doi.org/10.1029/jb081i023p04381>
- Aki, K., & Richards, P. G. (2002). Quantitative seismology.
- Albuquerque Seismological Laboratory (ASL)/USGS. (1980). US Geological Survey Networks. *International Federation of Digital Seismograph Networks*. <https://doi.org/10.7914/SN/GS>
- Albuquerque Seismological Laboratory (ASL)/USGS. (1990). United States National Seismic Network. *International Federation of Digital Seismograph Networks*. <https://doi.org/10.7914/SN/US>
- Ammon, C. J. (1991). The isolation of receiver effects from teleseismic P waveforms. *Bulletin of the Seismological Society of America*, 81(6), 2504–2510. <https://doi.org/10.1785/bssa0810062504>
- Audet, P. (2015). Layered crustal anisotropy around the San Andreas fault near Parkfield, California. *Journal of Geophysical Research: Solid Earth*, 120(5), 3527–3543. <https://doi.org/10.1002/2014jb011821>
- Bakun, W., Aagaard, B., Dost, B., Ellsworth, W. L., Hardebeck, J. L., Harris, R. A., et al. (2005). Implications for prediction and hazard assessment from the 2004 Parkfield earthquake. *Nature*, 437(7061), 969–974. <https://doi.org/10.1038/nature04067>
- Becken, M., Ritter, O., Bedrosian, P. A., & Weckmann, U. (2011). Correlation between deep fluids, tremor and creep along the central San Andreas fault. *Nature*, 480(7375), 87–90. <https://doi.org/10.1038/nature10609>
- Bleibinhaus, F., Hole, J. A., Ryberg, T., & Fuis, G. S. (2007). Structure of the California Coast Ranges and San Andreas Fault at SAFOD from seismic waveform inversion and reflection imaging. *Journal of Geophysical Research*, 112(B6), B06315. <https://doi.org/10.1029/2006jb004611>
- California Institute of Technology and United States Geological Survey Pasadena. (1926). Southern California Seismic Network. *International Federation of Digital Seismograph Networks*. <https://doi.org/10.7914/SN/CI>
- Chen, G., Chen, J., Li, T., Xu, M., Zhao, Q., & Tong, P. (2024). Adjoint-state reflection traveltime tomography for velocity and interface inversion with its application in central California near Parkfield. [Model] [Dataset]. Zenodo. <https://doi.org/10.5281/zenodo.14202376>
- Chen, J., Chen, G., Nagaso, M., & Tong, P. (2023). Adjoint-state traveltime tomography for azimuthally anisotropic media in spherical coordinates. *Geophysical Journal International*, 234(1), 712–736. <https://doi.org/10.1093/gji/ggad093>
- Christeson, G., Van Avendonk, H., Gulick, S., Reece, R., Pavlis, G., & Pavlis, T. (2013). Moho interface beneath Yakutat terrane, southern Alaska. *Journal of Geophysical Research: Solid Earth*, 118(9), 5084–5097. <https://doi.org/10.1002/jgrb.50361>
- Courant, R., Friedrichs, K., & Lewy, H. (1967). On the partial difference equations of mathematical physics. *IBM Journal of Research and Development*, 11(2), 215–234. <https://doi.org/10.1147/rd.112.0215>
- Dziewonski, A. M., Hager, B. H., & O'Connell, R. J. (1977). Large-scale heterogeneities in the lower mantle. *Journal of Geophysical Research*, 82(2), 239–255. <https://doi.org/10.1029/jb082i002p00239>
- Eberhart-Phillips, D., & Michael, A. J. (1993). Three-dimensional velocity structure, seismicity, and fault structure in the Parkfield region, central California. *Journal of Geophysical Research*, 98(B9), 15737–15758. <https://doi.org/10.1029/93jb01029>
- Fomel, S., Luo, S., & Zhao, H. (2009). Fast sweeping method for the factored eikonal equation. *Journal of Computational Physics*, 228(17), 6440–6455. <https://doi.org/10.1016/j.jcp.2009.05.029>
- Fornberg, B. (1988). The pseudospectral method; accurate representation of interfaces in elastic wave calculations. *Geophysics*, 53(5), 625–637. <https://doi.org/10.1190/1.1442497>
- Guo, G., Lan, H., Zhou, X., Liu, Y., Bin Waheed, U., & Chen, J. (2022). Topography-dependent eikonal tomography based on the fast-sweeping scheme and the adjoint-state technique. *Geophysics*, 87(2), U29–U41. <https://doi.org/10.1190/geo2021-0116.1>
- Guo, H., Zhang, H., Nadeau, R. M., & Peng, Z. (2017). High-resolution deep tectonic tremor locations beneath the San Andreas Fault near Cholame, California, using the double-pair double-difference location method. *Journal of Geophysical Research: Solid Earth*, 122(4), 3062–3075. <https://doi.org/10.1002/2016jb013919>
- Helmberger, D. V., Song, X., & Zhu, L. (2001). Crustal complexity from regional waveform tomography: Aftershocks of the 1992 Landers earthquake, California. *Journal of Geophysical Research*, 106(B1), 609–620. <https://doi.org/10.1029/2000jb900231>
- Hole, J., Ryberg, T., Fuis, G., Bleibinhaus, F., & Sharma, A. (2006). Structure of the San Andreas fault zone at SAFOD from a seismic refraction survey. *Geophysical Research Letters*, 33(7), L07312. <https://doi.org/10.1029/2005gl025194>
- Huang, J.-W., & Bellefleur, G. (2012). Joint transmission and reflection traveltime tomography using the fast sweeping method and the adjoint-state technique. *Geophysical Journal International*, 188(2), 570–582. <https://doi.org/10.1111/j.1365-246x.2011.05273.x>
- Hunter, J. D. (2007). Matplotlib: A 2D graphics environment. *Computing in Science & Engineering*, 9(3), 90–95. <https://doi.org/10.1109/mcse.2007.55>
- Institut de physique du globe de Paris (IPGP), & Ecole et Observatoire des Sciences de la Terre de Strasbourg (EOST). (1982). GEOSCOPE, French Global Network of broad band seismic stations. Institut de physique du globe de Paris (IPGP), Université de Paris. <https://doi.org/10.18715/GEOSCOPE.G>
- IRIS Transportable Array. (2003). USAArray Transportable Array. *International Federation of Digital Seismograph Networks*. <https://doi.org/10.7914/SN/TA>
- Jackson, J., McKenzie, D., & Priestley, K. (2021). Relations between earthquake distributions, geological history, tectonics and rheology on the continents. *Philosophical Transactions of the Royal Society A*, 379(2193), 20190412. <https://doi.org/10.1098/rsta.2019.0412>
- Jiang, C., Schmandt, B., Hansen, S. M., Dougherty, S. L., Clayton, R. W., Farrell, J., & Lin, F.-C. (2018). Rayleigh and S wave tomography constraints on subduction termination and lithospheric foundering in central California. *Earth and Planetary Science Letters*, 488, 14–26. <https://doi.org/10.1016/j.epsl.2018.02.009>
- Kao, C. Y., Osher, S., & Qian, J. (2004). Lax–Friedrichs sweeping scheme for static Hamilton–Jacobi equations. *Journal of Computational Physics*, 196(1), 367–391. <https://doi.org/10.1016/j.jcp.2003.11.007>
- Knapp, C. C., Knapp, J. H., & Connor, J. A. (2004). Crustal-scale structure of the South Caspian Basin revealed by deep seismic reflection profiling. *Marine and Petroleum Geology*, 21(8), 1073–1081. <https://doi.org/10.1016/j.marpetgeo.2003.04.002>
- Koene, E. F., Robertsson, J. O., Broggini, F., & Andersson, F. (2018). Eliminating time dispersion from seismic wave modeling. *Geophysical Journal International*, 213(1), 169–180. <https://doi.org/10.1093/gji/ggx563>
- Komatitsch, D., & Tromp, J. (1999). Introduction to the spectral element method for three-dimensional seismic wave propagation. *Geophysical Journal International*, 139(3), 806–822. <https://doi.org/10.1046/j.1365-246x.1999.00967.x>
- Lan, H., & Zhang, Z. (2013). Topography-dependent eikonal equation and its solver for calculating first-arrival traveltimes with an irregular surface. *Geophysical Journal International*, 193(2), 1010–1026. <https://doi.org/10.1093/gji/ggt036>

- Langston, C. A. (1979). Structure under Mount Rainier, Washington, inferred from teleseismic body waves. *Journal of Geophysical Research*, 84(B9), 4749–4762. <https://doi.org/10.1029/jb084ib09p04749>
- Leung, S., & Qian, J. (2006). An adjoint state method for three-dimensional transmission traveltimes tomography using first-arrivals.
- Li, T., Wu, S., & Tong, P. (2024). Multilevel transcrustal magmatic system beneath the Geysers-Clear Lake area. *Proceedings of the National Academy of Sciences*, 121(12), e2317809121. <https://doi.org/10.1073/pnas.2317809121>
- Li, T., Yao, J., Wu, S., Xu, M., & Tong, P. (2022). Moho complexity in southern California revealed by local PmP and teleseismic Ps waves. *Journal of Geophysical Research: Solid Earth*, 127(2), e2021JB023033. <https://doi.org/10.1029/2021jb023033>
- Lin, G., Thurber, C. H., Zhang, H., Hauksson, E., Shearer, P. M., Waldhauser, F., et al. (2010). A California statewide three-dimensional seismic velocity model from both absolute and differential times. *Bulletin of the Seismological Society of America*, 100(1), 225–240. <https://doi.org/10.1785/01200900028>
- Lions, J. L., & Magenes, E. (2012). *Non-homogeneous boundary value problems and applications: Vol. 1* (Vol. 181). Springer Science & Business Media.
- Lippoldt, R., Porritt, R. W., & Sammis, C. G. (2017). Relating seismicity to the velocity structure of the San Andreas Fault near Parkfield, CA. *Geophysical Journal International*, 209(3), 1740–1745. <https://doi.org/10.1093/gji/ggx131>
- Luo, S., & Qian, J. (2011). Factored singularities and high-order Lax–Friedrichs sweeping schemes for point-source traveltimes and amplitudes. *Journal of Computational Physics*, 230(12), 4742–4755. <https://doi.org/10.1016/j.jcp.2011.02.043>
- MASE. (2007). *Meso America Subduction Experiment*. Caltech. <https://doi.org/10.7909/C3RN35SP>
- Moore, D. E., & Rymer, M. J. (2007). Talc-bearing serpentinite and the creeping section of the San Andreas fault. *Nature*, 448(7155), 795–797. <https://doi.org/10.1038/nature06064>
- Nadeau, R. M., & Guilhem, A. (2009). Nonvolcanic tremor evolution and the San Simeon and Parkfield, California, earthquakes. *Science*, 325(5937), 191–193. <https://doi.org/10.1126/science.1174155>
- NCEDC. (2014). Northern California Earthquake Data Center [Dataset]. UC Berkeley Seismological Laboratory. <https://doi.org/10.7932/NCEDC>
- Northern California Earthquake Data Center. (2014). *Berkeley Digital Seismic Network (BDSN)*. Northern California Earthquake Data Center. <https://doi.org/10.7932/BDSN>
- Owens, T. J., Zandt, G., & Taylor, S. R. (1984). Seismic evidence for an ancient rift beneath the Cumberland Plateau, Tennessee: A detailed analysis of broadband teleseismic P waveforms. *Journal of Geophysical Research*, 89(B9), 7783–7795. <https://doi.org/10.1029/jb089ib09p07783>
- Ozacar, A. A., & Zandt, G. (2009). Crustal structure and seismic anisotropy near the San Andreas Fault at Parkfield, California. *Geophysical Journal International*, 178(2), 1098–1104. <https://doi.org/10.1111/j.1365-246x.2009.04198.x>
- Page, B. M., Coleman, R. G., & Thompson, G. A. (1998). Overview: Late Cenozoic tectonics of the central and southern Coast Ranges of California. *Geological Society of America Bulletin*, 110(7), 846–876. [https://doi.org/10.1130/0016-7606\(1998\)110<846:olctot>2.3.co;2](https://doi.org/10.1130/0016-7606(1998)110<846:olctot>2.3.co;2)
- Plessix, R.-E. (2006). A review of the adjoint-state method for computing the gradient of a functional with geophysical applications. *Geophysical Journal International*, 167(2), 495–503. <https://doi.org/10.1111/j.1365-246x.2006.02978.x>
- Podvin, P., & Lecomte, I. (1991). Finite difference computation of traveltimes in very contrasted velocity models: A massively parallel approach and its associated tools. *Geophysical Journal International*, 105(1), 271–284. <https://doi.org/10.1111/j.1365-246x.1991.tb03461.x>
- Rawlinson, N., & Sambridge, M. (2004a). Multiple reflection and transmission phases in complex layered media using a multistage fast marching method. *Geophysics*, 69(5), 1338–1350. <https://doi.org/10.1190/1.1801950>
- Rawlinson, N., & Sambridge, M. (2004b). Wave front evolution in strongly heterogeneous layered media using the fast marching method. *Geophysical Journal International*, 156(3), 631–647. <https://doi.org/10.1111/j.1365-246x.2004.02153.x>
- Riahi, M. A., & Juhan, C. (1994). 3-D interpretation of reflected arrival times by finite-difference techniques. *Geophysics*, 59(5), 844–849. <https://doi.org/10.1190/1.1443642>
- Salah, M. K., Zhao, D., Lei, J., & Abdelwahed, M. F. (2005). Crustal heterogeneity beneath southwest Japan estimated from direct and Moho-reflected waves. *Tectonophysics*, 395(1–2), 1–17. <https://doi.org/10.1016/j.tecto.2004.08.005>
- SCEDC. (2013). Southern California Earthquake Center [Dataset]. Caltech. <https://doi.org/10.7909/C3WD3xH1>
- Schmandt, B., Lin, F.-C., & Karlstrom, K. E. (2015). Distinct crustal isostasy trends east and west of the Rocky Mountain Front. *Geophysical Research Letters*, 42(23), 10–290. <https://doi.org/10.1002/2015gl066593>
- Sethian, J. A. (1999). Fast marching methods. *SIAM Review*, 41(2), 199–235. <https://doi.org/10.1137/s0036144598347059>
- Sethian, J. A., & Vladimirsky, A. (2000). Fast methods for the Eikonal and related Hamilton–Jacobi equations on unstructured meshes. *Proceedings of the National Academy of Sciences*, 97(11), 5699–5703. <https://doi.org/10.1073/pnas.090060097>
- Shelly, D. R. (2017). A 15 year catalog of more than 1 million low-frequency earthquakes: Tracking tremor and slip along the deep San Andreas Fault. *Journal of Geophysical Research: Solid Earth*, 122(5), 3739–3753. <https://doi.org/10.1002/2017jb014047>
- Shelly, D. R., & Hardebeck, J. L. (2010). Precise tremor source locations and amplitude variations along the lower-crustal central San Andreas Fault. *Geophysical Research Letters*, 37(14). <https://doi.org/10.1029/2010gl043672>
- Taillandier, C., Noble, M., Chauris, H., & Calandra, H. (2009). First-arrival traveltimes tomography based on the adjoint-state method. *Geophysics*, 74(6), WCB1–WCB10. <https://doi.org/10.1190/1.3250266>
- Tape, C., Liu, Q., Maggi, A., & Tromp, J. (2009). Adjoint tomography of the southern California crust. *Science*, 325(5943), 988–992. <https://doi.org/10.1126/science.1175298>
- Tessmer, E., Kosloff, D., & Behle, A. (1992). Elastic wave propagation simulation in the presence of surface topography. *Geophysical Journal International*, 108(2), 621–632. <https://doi.org/10.1111/j.1365-246x.1992.tb04641.x>
- Thomas, A. M., Nadeau, R. M., & Bürgmann, R. (2009). Tremor-tide correlations and near-lithostatic pore pressure on the deep San Andreas fault. *Nature*, 462(7276), 1048–1051. <https://doi.org/10.1038/nature08654>
- Thompson, J. F., Warsi, Z. U., & Mastin, C. W. (1985). *Numerical grid generation: Foundations and applications*. Elsevier North-Holland, Inc.
- Thurber, C., & Roecker, S. (2000). Parkfield passive seismic array. *International Federation of Digital Seismograph Networks*. [https://doi.org/10.7914/SN/XN\\_2000](https://doi.org/10.7914/SN/XN_2000)
- Thurber, C., & Roecker, S. (2004). Seismic tomography and location calibration around the SAFOD site. *International Federation of Digital Seismograph Networks*. [https://doi.org/10.7914/SN/YH\\_2004](https://doi.org/10.7914/SN/YH_2004)
- Thurber, C., Zhang, H., Waldhauser, F., Hardebeck, J., Michael, A., & Eberhart-Phillips, D. (2006). Three-dimensional compressional wavespeed model, earthquake relocations, and focal mechanisms for the Parkfield, California, region. *Bulletin of the Seismological Society of America*, 96(4B), S38–S49. <https://doi.org/10.1785/0120050825>
- Titus, S. J., DeMets, C., & Tikoff, B. (2006). Thirty-five-year creep rates for the creeping segment of the San Andreas fault and the effects of the 2004 Parkfield earthquake: Constraints from alignment arrays, continuous global positioning system, and creepmeters. *Bulletin of the Seismological Society of America*, 96(4B), S250–S268. <https://doi.org/10.1785/0120050811>

- Tong, P. (2021a). Adjoint-state traveltome tomography: Eikonal equation-based methods and application to the Anza area in southern California. *Journal of Geophysical Research: Solid Earth*, 126(5), e2021JB021818. <https://doi.org/10.1029/2021jb021818>
- Tong, P. (2021b). Adjoint-state traveltome tomography for azimuthally anisotropic media and insight into the crustal structure of central California near Parkfield. *Journal of Geophysical Research: Solid Earth*, 126(10), e2021JB022365. <https://doi.org/10.1029/2021jb022365>
- Tong, P., Yang, D., & Huang, X. (2019). Multiple-grid model parametrization for seismic tomography with application to the San Jacinto fault zone. *Geophysical Journal International*, 218(1), 200–223. <https://doi.org/10.1093/gji/ggz151>
- Trabant, C., Hutko, A. R., Bahavar, M., Karstens, R., Ahern, T., & Aster, R. (2012). Data products at the IRIS DMC: Stepping stones for research and other applications. *Seismological Research Letters*, 83(5), 846–854. <https://doi.org/10.1785/0220120032>
- Tsai, Y.-H. R., Cheng, L.-T., Osher, S., & Zhao, H.-K. (2003). Fast sweeping algorithms for a class of Hamilton–Jacobi equations. *SIAM Journal on Numerical Analysis*, 41(2), 673–694. <https://doi.org/10.1137/s0036142901396533>
- Turner, R. C., Shirzaei, M., Nadeau, R. M., & Bürgmann, R. (2015). Slow and Go: Pulsing slip rates on the creeping section of the San Andreas Fault. *Journal of Geophysical Research: Solid Earth*, 120(8), 5940–5951. <https://doi.org/10.1002/2015jb011998>
- Van der Hilst, R. D., Widjiantoro, S., & Engdahl, E. (1997). Evidence for deep mantle circulation from global tomography. *Nature*, 386(6625), 578–584. <https://doi.org/10.1038/386578a0>
- Vernon, F., & Orcutt, J. (2010). MARS/Testing of cabled broadband OBS using MARS test facility. *International Federation of Digital Seismograph Networks*. [https://doi.org/10.7914/SN/4E\\_2010](https://doi.org/10.7914/SN/4E_2010)
- Waldhauser, F., & Schaff, D. P. (2008). Large-scale relocation of two decades of Northern California seismicity using cross-correlation and double-difference methods. *Journal of Geophysical Research*, 113(B8). <https://doi.org/10.1029/2007jb005479>
- Wang, D., Wu, S., Li, T., Tong, P., & Gao, Y. (2022). Elongated magma plumbing system beneath the Coso volcanic field, California, constrained by seismic reflection tomography. *Journal of Geophysical Research: Solid Earth*, 127(6), e2021JB023582. <https://doi.org/10.1029/2021jb023582>
- Wessel, P., Luis, J. F., Uieda, L. a., Scharroo, R., Wobbe, F., Smith, W. H., & Tian, D. (2019). The generic mapping tools version 6. *Geochemistry, Geophysics, Geosystems*, 20(11), 5556–5564. <https://doi.org/10.1029/2019gc008515>
- Wu, S., Li, T., Wang, D., & Tong, P. (2022). Lower crust structures and dynamics of southern California revealed by first P and PmP traveltome data. *Tectonophysics*, 830, 229328. <https://doi.org/10.1016/j.tecto.2022.229328>
- Xia, S., Zhao, D., Qiu, X., Nakajima, J., Matsuzawa, T., & Hasegawa, A. (2007). Mapping the crustal structure under active volcanoes in central Tohoku, Japan using P and PmP data. *Geophysical Research Letters*, 34(10). <https://doi.org/10.1029/2007gl030026>
- Zeng, X., Thurber, C. H., Shelly, D. R., Harrington, R. M., Cochran, E. S., Bennington, N. L., et al. (2016). 3-D P- and S-wave velocity structure and low-frequency earthquake locations in the Parkfield, California region. *Geophysical Journal International*, 206(3), 1574–1585. <https://doi.org/10.1093/gji/ggw217>
- Zhang, H., Nadeau, R. M., & Guo, H. (2017). Imaging the nonvolcanic tremor zone beneath the San Andreas fault at Cholame, California using station-pair double-difference tomography. *Earth and Planetary Science Letters*, 460, 76–85. <https://doi.org/10.1016/j.epsl.2016.12.006>
- Zhao, D., Todo, S., & Lei, J. (2005). Local earthquake reflection tomography of the Landers aftershock area. *Earth and Planetary Science Letters*, 235(3–4), 623–631. <https://doi.org/10.1016/j.epsl.2005.04.039>
- Zhao, H. (2005). A fast sweeping method for eikonal equations. *Mathematics of Computation*, 74(250), 603–627. <https://doi.org/10.1090/s0025-5718-04-01678-3>
- Zhou, X., Lan, H., Chen, L., Guo, G., Bin Waheed, U., & Badal, J. (2023). A topography-dependent eikonal solver for accurate and efficient computation of traveltimes and their derivatives in 3D heterogeneous media. *Geophysics*, 88(2), U17–U29. <https://doi.org/10.1190/geo2021-0799.1>
- Zhu, H., Bozdağ, E., Peter, D., & Tromp, J. (2012). Structure of the European upper mantle revealed by adjoint tomography. *Nature Geoscience*, 5(7), 493–498. <https://doi.org/10.1038/ngeo1501>
- Zhu, L., & Kanamori, H. (2000). Moho depth variation in southern California from teleseismic receiver functions. *Journal of Geophysical Research*, 105(B2), 2969–2980. <https://doi.org/10.1029/1999jb900322>

## References From the Supporting Information

- Crotwell, H. P., Owens, T. J., & Ritsema, J. (1999). The TauP Toolkit: Flexible seismic travel-time and ray-path utilities. *Seismological Research Letters*, 70(2), 154–160. <https://doi.org/10.1785/gssr.70.2.154>
- James, D. E., Niemi, F., & Rokosky, J. (2003). Crustal structure of the Kaapvaal craton and its significance for early crustal evolution. *Lithos*, 71(2–4), 413–429. <https://doi.org/10.1016/j.lithos.2003.07.009>
- Nakajima, J., Matsuzawa, T., & Hasegawa, A. (2002). Moho depth variation in the central part of northeastern Japan estimated from reflected and converted waves. *Physics of the Earth and Planetary Interiors*, 130(1–2), 31–47. [https://doi.org/10.1016/s0031-9201\(01\)00307-7](https://doi.org/10.1016/s0031-9201(01)00307-7)
- Tromp, J., Komatitsch, D., & Liu, Q. (2008). Spectral-element and adjoint methods in seismology. *Communications in Computational Physics*, 3(1), 1–32.